

CONSTRANED LOCAL APPROXIMATE IDEAL RESTRICTION FOR ADVECTION-DIFFUSION PROBLEMS*

AHSAN ALI[†], JAMES J. BRANNICK[‡], KARSTEN KAHL[§], OLIVER A. KRZYSIK[¶], JACOB B. SCHRODER^{||},
AND BEN S. SOUTHWORTH[#]

Abstract. This paper focuses on developing a reduction-based algebraic multigrid (AMG) method that is suitable for solving general (non)symmetric linear systems and is naturally robust from pure advection to pure diffusion. Initial motivation comes from a new reduction-based algebraic multigrid approach, ℓ AIR (local approximate ideal restriction), that was developed for solving advection-dominated problems. Though this new solver is very effective in the advection dominated regime, its performance degrades in cases where diffusion becomes dominant. This is consistent with the fact that in general, reduction-based AMG methods tend to suffer from growth in complexity and/or convergence rates as the problem size is increased, especially for diffusion dominated problems in two or three dimensions. Motivated by the success of ℓ AIR in the advective regime, our aim in this paper is to generalize the AIR framework with the goal of improving the performance of the solver in diffusion dominated regimes. To do so, we propose a novel way to combine mode constraints as used commonly in energy minimization AMG methods with the local approximation of ideal operators used in ℓ AIR. The resulting constrained ℓ AIR ($\mathcal{C}\ell$ AIR) algorithm is able to achieve fast scalable convergence on advective and diffusive problems. In addition, it is able to achieve standard low complexity hierarchies in the diffusive regime through aggressive coarsening, something that has been previously difficult for reduction-based methods.

Key words. algebraic multigrid, multigrid reduction, root-node, energy minimization, nonsymmetric, preconditioning

MSC codes. 65N55, 65N22, 65F08, 65F10

1. Introduction. We design and analyze a reduction-based algebraic multigrid (rAMG) algorithm for linear systems of algebraic equations

$$(1.1) \quad A\mathbf{u} = \mathbf{f},$$

where $A \in \mathbb{R}^{n \times n}$ is assumed to be a sparse nonsymmetric matrix. Our focus in this paper is on solving (1.1) arising from discretizations of advection-diffusion-reaction partial differential equations (PDEs), which arise in various practical applications and also serve as interesting initial model problems for testing nonsymmetric AMG solvers. Ultimately, our objective is a method that is naturally robust and efficient in both the advection and diffusion limits.

Multigrid methods for solving (1.1) use a relaxation process or smoother, defined in this paper by M , as a local solver for a sequence of coarse-level systems of equations to reduce the global error resulting from applying relaxation on the finest level. In AMG, a recursive two-level point of view is often used, both in terms of the development of the AMG setup algorithm as well as the analysis of the solver it produces. In this two-level context, the idea is to analyze two complementary processes to efficiently solve sparse linear systems, a relaxation scheme on the fine-level, with corresponding error propagation matrix given by $I - M^{-1}A$, and a coarse-level correction, with error propagation matrix given by $I - PA_c^{-1}RA$. Here, $P \in \mathbb{R}^{n \times n_c}$, $n_c < n$, denotes the interpolation matrix that maps corrections from the coarse-level, $R \in \mathbb{R}^{n_c \times n}$ is the restriction matrix that maps residuals to the coarse-level, and $A_c = RAP$ is the coarse-level operator. The error propagation matrix of the resulting two-level method, from which a multilevel method is defined recursively, reads

$$E_{TG} = (I - M^{-1}A)(I - PA_c^{-1}RA).$$

The AMG solver is then defined from this two-level scheme by recursively applying it on the coarse-level to approximate A_c^{-1} , and reduce the errors remaining after applying relaxation on the finer levels.

In AMG, the smoother M is typically fixed to be a simple point-wise method and then R and P are constructed in an automated setup algorithm that takes as input the system matrix A . In this paper,

*Submitted to the editors June 30, 2023.

Funding: This work was funded by NSF grants DMS-2110917 and DMS-2111219.

[†]Department of Mathematics and Statistics, University of New Mexico, Albuquerque, NM, USA (ahsan@unm.edu)

[†]Department of Mathematics, Penn State University, University Park, PA, USA (jjb23@psu.edu)

[§]School of Mathematics and Natural Sciences, Bergische Universität Wuppertal, Wuppertal, Germany (kkahl@uni-wuppertal.de)

[¶]Department of Applied Mathematics, University of Waterloo, Waterloo, Ontario, Canada (okrzysik@uwaterloo.ca)

Department of Mathematics and Statistics, University of New Mexico, Albuquerque, NM, USA (jbschroder@unm.edu)

#Los Alamos National Laboratory, Los Alamos, NM, USA (southworth@lanl.gov)

44 since we consider a reduction-based AMG framework, we assume that the smoother is a point-wise F -
 45 relaxation scheme, where the set F denotes the set of fine variables in the coarse-fine (C/F) splitting
 46 of the degrees of freedom Ω such that $C \cup F = \Omega$ and $C \cap F = \emptyset$. In this setting, the main tasks
 47 in the AMG setup algorithm are to construct the restriction and interpolation matrices R and P such
 48 that certain *approximation properties* hold and R and P (and thus $A_c = RAP$) are *sparse* matrices.
 49 The latter sparsity requirement implies that the setup procedure can be efficiently applied recursively
 50 to $A_c = RAP$ in order to construct an optimal multilevel AMG solver.

51 In the SPD case, the variational choice $R = P^T$ is used and the weak approximation property for P
 52 bounds the convergence rate of the two-level method in the A -norm. Notably, the weak approximation
 53 property has as its minimizer the so-called ideal interpolation matrix [12]. This ideal form of interpolation
 54 gives rise to the Schur-complement of A as the coarse-level system matrix and, thus, coincides with block
 55 Gaussian elimination based on the given coarse-fine splitting. In contrast to classical AMG methods
 56 that use a global smoother in the AMG solver (e.g., weighted-Jacobi or lexicographic Gauss-Seidel),
 57 reduction based methods that are motivated by this block factorization interpretation choose smoothers
 58 that focus on the subspace defined by the fine variables F .

59 Traditionally, classical AMG methods are very effective for sparse SPD problems, e.g., discretiza-
 60 tions of various diffusion and heat conduction problems, and not as effective for nonsymmetric problems,
 61 whereas, reduction-based AMG methods have been developed that work well for nonsymmetric prob-
 62 lems with a near-triangular (upwinded) structure, e.g., space-time discretizations [26] and advection-
 63 dominated PDEs [20, 18]. The parallel-in-time method called multigrid reduction in time (MGRIT) [11]
 64 is another recent application of reduction-based multigrid methods, where time integration is recognized
 65 as suitable for reduction-based approaches because time is one-dimensional and optimal coarsening is
 66 practical; however, MGRIT differs from rAMG methods in using a non-Galerkin coarse grid typically
 67 based on rediscretization in time. Interestingly, theory [27, 10, 29] (and practice) has indicated that
 68 without special care (e.g., [9]) MGRIT is effective on space-time PDEs with parabolic problems, partic-
 69 ularly SPD spatial discretizations, but struggles with hyperbolic PDEs and highly nonsymmetric spatial
 70 discretizations.

71 Indeed, solving more general non-symmetric systems arising from higher dimensional spatial PDEs
 72 or space-time PDEs is more complicated in terms of balancing the convergence and complexity of a
 73 multilevel solver. A viable approach for solving the latter higher dimensional problems is given by
 74 the ℓ AIR solver [20]. The approach has been extensively studied and tested for analogous advection-
 75 diffusion-reaction model problems we consider here [21, 18, 20], and also demonstrated on more complex
 76 advection-dominated physics, e.g., [28, 8]. In general, ℓ AIR performs very well for advection-dominated
 77 problems, with performance more mixed for diffusive problems, i.e., for problems with strong diffusion
 78 ℓ AIR suffers from degraded convergence and similar complexity issues as other reduction-based AMG
 79 methods for diffusion type problems in higher dimensions. We mention the recent paper [32] which
 80 represents the state-of-the-art in research on techniques for improving the performance of reduction-
 81 based AMG solvers for diffusion problems. There, the traditional approach of constructing a row-wise
 82 approximation of ideal interpolation is considered and the focus is on improving approximations to A_{ff}^{-1}
 83 using sparse approximate inverse techniques, similar to the sparse Krylov approximations that have been
 84 studied, and very recently used for a highly efficient parallel variation of ℓ AIR [8].

85 In this paper, we combine the reduction-based principles of ℓ AIR with the mode constraints of energy-
 86 minimization AMG [17, 31, 6, 22, 25, 19]. The ℓ AIR algorithm offers sparse, accurate approximations of
 87 ideal transfer operators in the strongly advective regime, which also yields excellent AMG approximation
 88 properties [21]. In contrast, in diffusive regimes, accurate and sparse approximations of ideal transfer
 89 operators are generally not viable due to the density of A_{ff}^{-1} ; because no other information is taken into
 90 account, the AMG approximation properties of ℓ AIR also suffer or the complexity must dramatically
 91 increase. Classical and energy-minimization AMG methods suffer from the opposite problem – they tend
 92 to offer excellent AMG approximation properties for diffusive problems, but very poor approximation
 93 properties in the advective regime [21]. On a high level, this is because the near nullspace of advective
 94 operators cannot be represented simply by smoothed constant vectors, the basis for almost all classical
 95 AMG and energy minimization methods. Energy minimization methods inadvertently further block their
 96 potential by using some form of normal equations to perform energy minimization in the nonsymmetric
 97 setting (wherein the nonsymmetric matrix A does not define a natural energy or minimization). Such
 98 minimization converges to the ideal transfer operators of the *normal equations* [19], even though a sparse
 99 accurate approximation of ideal transfer operators is often viable for matrix A , which ℓ AIR successfully

100 targets.

101 Here, we recognize this subtlety in approximation properties that guides the success of different
 102 AMG methods in different regimes, and define a new constrained variation of the ℓ AIR algorithm.
 103 Constrained ℓ AIR (C ℓ AIR) directly approximates the ideal transfer operators using a similar objective
 104 as in ℓ AIR, while constraining the range of P or R^T to include known or expected near-null space
 105 mode(s), thereby harnessing the power of reduction-based and energy-minimization methods in their
 106 respective regimes. In relaxation, we restrict ourselves to simple F - and C -point Jacobi relaxation,
 107 demonstrating that with careful construction of transfer operators, we are able to apply an efficient
 108 reduction-based method for diffusive-dominated problems. As it turns out, the construction of sparsity
 109 patterns for transfer operators in ℓ AIR and root-node based energy minimization [19] are very similar
 110 in principle, namely that they are defined column-wise for P and row-wise for R . As a result, we are
 111 also able to naturally incorporate an aggressive root-node approach to choosing coarse variables [25, 19]
 112 for diffusion dominated problems, ameliorating the (necessarily) high complexity that tends to arise in
 113 reduction-based and advective solvers [20].

114 In the case of anisotropic diffusion, we observe that the energy minimization approach depends
 115 crucially on the aggressive root-node coarsening technique [25]. In this case, the aggressive coarsening
 116 selects a relatively small number of coarse variables to compensate for the complexity of the long-
 117 range interpolation required for the non-grid aligned anisotropy [25]. The outcome is a low-complexity,
 118 effective AMG solver. By combining neighborhoods of fine degrees of freedom (DOFs) into a single
 119 coarse variable, root-node accomplishes this by greedy aggregation [30], in which the seed point of each
 120 aggregate becomes the C -point (root-node) and the remaining degrees of freedom become F -points.
 121 The member points (F and C) of each aggregate define the initial nonzero pattern of the corresponding
 122 column of P . Generally speaking, this greedy aggregation procedure places C -points farther apart than
 123 the traditional Ruge-Stüben (RS) C/F -splitting of the fine degrees of freedom. This results in a more
 124 aggressive coarsening and fewer coarse variables (i.e., lower complexity) for root-node [25, 19]. The
 125 column-wise viewpoint that we employ in the definition of C ℓ AIR interpolation allows us to similarly
 126 use aggressive root-node coarsening to control complexity, particularly for diffusive problems, and to
 127 also incorporate constraint vectors for improved AMG convergence that are fit into $\text{span}(P)$ (similar to
 128 smoothed aggregation methods [30, 19]).

129 This paper is organized as follows. The next section reviews reduction-based AMG and the ℓ AIR
 130 framework that motivates our new method, and provides practical connections to energy minimization
 131 AMG methods that facilitate our method design. Our new method C ℓ AIR is presented in Section 3,
 132 and Section 4 contains numerical results that illustrate the performance of our algorithms applied to
 133 various discretizations of our model advection-diffusion problem. In particular, C ℓ AIR is able to maintain
 134 fast robust convergence on advection-dominated problems, while also yielding low-complexity scalable
 135 solutions for diffusion dominated problems. To complement the numerical results for the proposed
 136 method C ℓ AIR, we present a study of classical AMG weak and strong approximation properties in
 137 Appendix A.

138 **2. Reduction based AMG and ℓ AIR interpolation.** Let $A \in \mathbb{R}^{n \times n}$ and assume that the
 139 degrees of freedom $\Omega = \{1, \dots, n\}$ are partitioned in the classical sense such that we have n_c C -points
 140 and n_f F -points. Then, A can be represented in the following block form:

$$141 \quad (2.1) \quad A = \begin{pmatrix} A_{ff} & A_{fc} \\ A_{cf} & A_{cc} \end{pmatrix}.$$

143 As before, define $P : \mathbb{R}^{n_c} \mapsto \mathbb{R}^n$ and $R : \mathbb{R}^n \mapsto \mathbb{R}^{n_c}$ as interpolation and restriction respectively. Further,
 144 assume that C -points are interpolated and restricted by injection in the classical AMG sense; then, the
 145 transfer operators P and R in reduction based AMG can be written in the following block form:

$$146 \quad (2.2) \quad P = \begin{pmatrix} W \\ I \end{pmatrix}, \quad R = (Z \quad I),$$

148 where the ordering here is useful in formalizing a reduction-based AMG method. Design of classical
 149 reduction based AMG methods is motivated by the observation that the ideal interpolation operator is
 150 the unique operator

$$151 \quad (2.3) \quad P_{\text{ideal}} = \begin{pmatrix} -A_{ff}^{-1}A_{fc} \\ I \end{pmatrix}$$

153 that eliminates the contribution of the coarse-grid correction \mathbf{e}_c to the F -point residual:

154 (2.4)
$$AP\mathbf{e}_c = \begin{pmatrix} \mathbf{0} \\ S\mathbf{e}_c \end{pmatrix}.$$

 155

156 Assuming R and P take the form of (2.2), we have independent of A that the Petrov-Galerkin coarse
 157 grid satisfies $RAP = S := A_{cc} - A_{cf}A_{ff}^{-1}A_{fc}$, where S is the Schur complement [12, 20].

158 Reduction based methods for diffusion type problems have traditionally assumed the classical AMG
 159 form of interpolation in (2.3) and approximate $-A_{ff}^{-1}A_{fc}$ by solving for each $i \in C$

160 (2.5)
$$A_{ff}W^{[i]} = -A_{fc}^{[i]},$$

 161

162 for the n_c columns of the interpolation weight matrix W defined as in (2.2). Here, we use the notation
 163 $X^{\{i\}}$ to refer to the i th row of a matrix X , whereas, $X^{[i]}$ will denote a column of the matrix. In this
 164 classical reduction-based setting, choosing the coarse grid degrees of freedom C as well as choosing the
 165 sparsity structure of the rows of W are done using classical AMG coarsening and strength of connection
 166 heuristics and the resulting algorithms typically lead to high grid and operator complexities, even when
 167 very simple approximations of A_{ff}^{-1} are used. We mention that various approximations to A_{ff}^{-1} in the
 168 computation of P and in relaxation are possible and have been considered in the literature, and we
 169 reiterate that in our development we focus on designing an approach that achieves both low grid and
 170 operator complexities while at the same time only requiring the simplest diagonal (Jacobi) F-relaxation
 171 scheme for fast convergence.

172 **2.1. Review of ℓ AIR.** The ℓ AIR approach that we build our new method around is based on the
 173 similar observation that the ideal restriction operator is the unique operator [20]

174 (2.6)
$$R_{\text{ideal}} = (-A_{cf}A_{ff}^{-1} \quad I)$$

 175

176 that eliminates all error at F -points:

177 (2.7)
$$RA \begin{pmatrix} \delta\mathbf{e}_f \\ \mathbf{0} \end{pmatrix} = \mathbf{0} \quad \forall \delta\mathbf{e}_f.$$

 178

179 Here, the ordering of the equations is again based on a splitting of $\Omega = C \cup F$. The ℓ AIR approach is
 180 then based on setting RA equal to zero in (2.7) within a pre-determined F -point sparsity pattern for Z .
 181 A similar method to approximate ideal interpolation can be expressed as satisfying $AP = 0$ exactly a
 182 specified sparsity pattern for W . Note that the AIR approach can also be seen as directly approximating
 183 the action of R_{ideal} on F -points, where $R_{\text{ideal}}A = (\mathbf{0}, S)$, for the Schur complement S . Expressing this
 184 result in terms of some matrix Z , the approach is equivalent to satisfying

185 (2.8)
$$ZA_{ff} = -A_{cf}$$

 186

187 within a predetermined sparsity pattern for Z . Here, the AIR approach is clearly different from the
 188 classical (reduction) AMG [4, 24, 16, 13] approach in that (2.8) involves solving for the n_c rows of Z (or
 189 R), which now gives a column-wise view of computing R^T and thereby an ℓ AIR style form of P .¹

190 Denoting indices of the sparsity pattern for the i th row of Z as $\mathcal{Z}_i = \{\ell_1, \dots, \ell_{S_i}\}$, where $S_i = |\mathcal{Z}_i|$ is
 191 the size of the sparsity pattern, the resulting (transposed) linear system for Z takes the form

191 (2.9)
$$\begin{pmatrix} a_{\ell_1\ell_1} & a_{\ell_2\ell_1} & \dots & a_{\ell_{S_i}\ell_1} \\ a_{\ell_1\ell_2} & a_{\ell_2\ell_2} & \dots & a_{\ell_{S_i}\ell_2} \\ \vdots & & \ddots & \vdots \\ a_{\ell_1\ell_{S_i}} & a_{\ell_2\ell_{S_i}} & \dots & a_{\ell_{S_i}\ell_{S_i}} \end{pmatrix} \begin{pmatrix} z_{i\ell_1} \\ z_{i\ell_2} \\ \vdots \\ z_{i\ell_{S_i}} \end{pmatrix} = - \begin{pmatrix} a_{i\ell_1} \\ a_{i\ell_2} \\ \vdots \\ a_{i\ell_{S_i}} \end{pmatrix}.$$

 192

¹We note that the reduction-based AMG approaches [16, 13] have also previously explored the use of constraint vector(s), however in addition to our different column-wise view of computing R^T , these approaches use cheap approximations to A_{ff}^{-1} (e.g., diagonal) with a more expensive multilevel adaptive approach for generating the constraint vector. In this work, we take the more expensive ℓ AIR approach to approximating A_{ff}^{-1} based on small block inverses, but combine that with a cheap constraint vector similar to energy-minimization methods, which require only a few relaxation sweeps on each level for improvement.

193 As demonstrated in [20, 18], for upwinded advection-dominated problems, very good sparse approximations to A_{ff}^{-1} can be made, which means that satisfying (2.8) within a sparsity pattern provides an
 194 accurate approximation to R_{ideal} . For advection-dominated problems, this approach also provides very
 195 good approximation properties of the resulting restriction operator, as demonstrated in [21] and the
 196 numerical results. In contrast, relying only on solving (2.8) for a diffusion dominated problem is unlikely
 197 to be effective, because A_{ff}^{-1} is generally more dense in this setting and not well approximated by a sparse
 198 matrix. Hand-in-hand with this, the resulting approximation properties are also poor. This has been
 199 mitigated reasonably well by combining ℓ AIR restriction with classical AMG interpolation for problems
 200 with strong diffusion, but the complexity remains high and convergence sub-par compared with classical
 201 AMG or energy minimization methods.

203 **2.2. Review of Root-node AMG.** One way to conceptualize root-node AMG [19] is as a combi-
 204 nation of classical and aggregation-based multigrid methods. Root-node AMG employs a hybrid strategy
 205 in which smoothed aggregation type strength-of-connection is used and aggregates are created using stan-
 206 dard aggregation routines. One node is selected as the ‘root-node’ in each aggregate which corresponds
 207 to a C -point, while all other nodes in the aggregate are identified as F -points. After that, transfer
 208 operators are created in the following manner.

209 Root-node utilizes algebraically smoothed candidates B , which are fit into the span of interpolation,
 210 and in order to recurse, coarse versions, B_c , of the candidates are obtained by injecting B to the C -
 211 points. Next, the initial tentative interpolation T is formed by injecting only the first q candidates over
 212 each aggregate, where q is the block size of the original matrix ($q = 1$ for a scalar problem). On the
 213 coarse grid, each root-node thus represents q DOFs. On T , a further step is taken to normalize every
 214 column. This procedure produces the following form

$$215 \quad (2.10) \quad T = \begin{pmatrix} W \\ I \end{pmatrix} \begin{array}{l} \{ \text{Non Root-nodes} \\ \{ \text{Root-nodes} \end{array}$$

216 For $q = 1$, T has non-overlapping columns; for $q > 1$, W is block diagonal.

217 The remaining candidates are projected into $\text{range}(T)$ in the Euclidean inner-product if there are
 218 more than q candidates. It is expected in root-node AMG that the allowed sparsity pattern of T has
 219 enough DOFs to make this an underdetermined problem. The sparsity pattern of T is typically grown
 220 with strength of connection information, as we later do for $C\ell$ AIR. Consequently, a minimal norm update
 221 is applied to each row of T , guaranteeing that $TB_c = B$ and T adheres to the sparsity pattern. The
 222 interpolation P is then generated using subsequent energy-minimization updates to T (briefly covered
 223 in the following subsection). Root-node minimizes energy by solving $A \begin{pmatrix} W \\ I \end{pmatrix} = 0$ subject to the mode
 224 interpolation constraints so that the solution is non zero.

225 **2.3. Energy minimization and mode constraints.** Another well-known class of AMG methods
 226 is that of energy-minimization. We will particularly focus on root-node energy-minimization [19], which
 227 shares the CF-splitting design of reduction-based methods. One key part of energy-minimization is the
 228 use of constraints during the minimization process. For efficiency reasons, the sparsity pattern of P is
 229 constrained. Let \mathcal{W} be the sparsity pattern for the F-rows in P . We denote that P obeys the sparsity
 230 pattern constraint with

$$231 \quad (2.11) \quad P \in [\mathcal{W} \ I] \quad \text{or} \quad W \in \mathcal{W}.$$

232 For approximation property reasons, a near nullspace mode constraint is also typically enforced where

$$233 \quad (2.12) \quad B \in \text{span}(P),$$

234 and $B \in \mathbb{R}^{n,k}$ is a set of k global near nullspace modes. With P of the form (2.2) and equation (2.12),
 235 this then implies that $B_c = [0 \ I]B$, i.e., the fine-grid B is injected to the coarse-grid, along with the
 236 constraint,

$$237 \quad (2.13) \quad PB_c = B.$$

238 Similar to ℓ AIR, energy-minimization AMG takes a column-oriented view. Letting $P^{[j]}$ denote
 239 column j , construction of transfer operators is based around a minimization along the lines of

$$240 \quad (2.14) \quad P = \underset{P}{\text{argmin}} \sum_j \|P^{[j]}\|_{\mathcal{X}}^2, \text{ such that constraints (2.13) and (2.11) are satisfied,}$$

241 where \mathcal{X} denotes some norm, usually A for SPD operators or A^*A for nonsymmetric matrices. This
 242 column-oriented view is analogous to ℓ AIR in (2.9), but here we are minimizing in some energy-induced
 243 inner product, rather than solving each block equation exactly as in ℓ AIR.

244 Interestingly, this distinction has more profound consequences for the efficacy of the methods. For
 245 SPD operators, root-node uses projected conjugate gradients (CG) for equation (2.14); without con-
 246 straints (2.13) and (2.11), such a minimization procedure converges to P_{ideal} for A [19, Lemma 4.2].
 247 However in the nonsymmetric case, root-node uses a projected generalized minimal residual (GMRES)
 248 for equation (2.14), which in turn (without constraints (2.13) and (2.11)), converges to P_{ideal} for A^*A
 249 [19, Lemma 4.6]. Indeed, by posing the unconstrained problem as an (overdetermined) minimization,
 250 root-node is required to define an energy-induced inner product through the normal equations, which in
 251 turn leads to the approximation of P_{ideal} for the normal equations rather than directly for the operator of
 252 interest. In contrast, the base algorithm of ℓ AIR directly approximates (and converges to) P_{ideal} for the
 253 original operator A . This is possible because the algorithm is built around local matrix approximation
 254 (2.8) rather than a matrix-induced norm, which does not naturally exist for non-SPD matrices.

255 As it turns out, which ideal operators we are trying to approximate (without constraints) is an
 256 important distinction for highly advective problems, which typically generate discretization matrices
 257 that are close to block lower-triangular in some ordering [18]. For such cases [18], ℓ AIR achieves good
 258 sparse approximations to A_{ff}^{-1} for computing R_{ideal} and overall excellent AMG convergence. However if
 259 one were to approximate ideal transfer operators based on A^*A instead of A , the block lower-triangular
 260 structure that is key to achieving sparse and accurate approximations to A_{ff}^{-1} and R_{ideal} is completely
 261 lost. The natural result is that a good sparse approximation to A_{ff}^{-1} becomes more difficult to compute
 262 (see [18], Section 4 for more discussion), and the resulting AMG method is significantly less effective.
 263 Thus although the underlying problem that energy-minimization is based around, namely approximating
 264 $AP = \mathbf{0}$, is almost equivalent to ℓ AIR, by formulating via energy minimization the resulting class of
 265 methods yield lackluster performance on highly advective problems.

266 **2.4. The best of both worlds.** Looking carefully at the ℓ AIR and energy-minimization ap-
 267 proaches leads us to consider a new interpretation combining the best of both worlds. By directly
 268 approximating R_{ideal} of the original operator A , ℓ AIR is able to construct highly effective transfer oper-
 269 ators for advection-dominated problems; in contrast, mode constraints are fundamental to the efficacy
 270 of energy-minimization methods for diffusion dominated problems (indeed, without constraints energy
 271 minimization alone is generally not effective). Although ℓ AIR is based around approximation of ideal
 272 transfer operators, we can also think in terms of approximation properties – consider each row of R as
 273 the local fine-grid mode being restricted to a given C-point, where these modes should be local represen-
 274 tations of the smooth error. This is exactly what happens in classical smoothed aggregation [30], as well
 275 as when bilinear interpolation is used in geometric MG for diffusion. Thus we propose a new constrained
 276 ℓ AIR ($\mathcal{C}\ell$ AIR) method that is built around directly approximating the ideal transfer operators of A in
 277 an ℓ AIR framework, regardless of whether A is SPD or nonsymmetric, while also incorporating mode
 278 constraints as in energy minimization to improve robustness in diffusion dominated problems.

279 In summary, the proposed $\mathcal{C}\ell$ AIR approach combines strengths of root-node and ℓ AIR, with the goal
 280 of a robust solver in both the advective and diffusive regimes. The $\mathcal{C}\ell$ AIR approach for constructing ℓ AIR
 281 interpolation with constraints is directly related to solving (2.8) and thus is a constrained approximation
 282 of P_{ideal} for the original operator, in contrast to root-node, which targets the normal equations in the
 283 nonsymmetric setting. Also, all of our proposed generalizations can be used to build R and/or P .

284 **3. Constrained ℓ AIR transfer operators.** The main goals of our new reduction-based AMG
 285 method built around ℓ AIR-style interpolation, is to have a solver that (i) works well for both advection
 286 and diffusion problems, (ii) allows for the incorporation of mode interpolation constraints (local or
 287 global), and (iii) controls complexity in a reduction setting for diffusive problems through an aggressive
 288 root-node coarsening. To achieve these goals, we consider mixing ideas from ℓ AIR, which works well for
 289 advection, with energy-minimization and smoothed aggregation (SA) [30], which work well for anisotropic
 290 diffusion problems and allow for mode constraints. Another key component of the algorithm for diffusion
 291 dominated problems, described in detail in a latter section, is our use of a root-node aggregation-based
 292 coarsening algorithm.

293 The overall ℓ AIR interpolation scheme we consider is described as follows. Similar to the energy-
 294 minimization discussion above, we will enforce that P obeys the sparsity pattern constraint (2.11).
 295 Regarding the sparsity pattern \mathcal{W} for the F -rows, let \mathcal{W}_i denote the sparsity pattern for the i th column

296 of W , that is $\mathcal{W}_i = \{m_1, \dots, m_{T_i}\}$ and the number of nonzeros in column i equals $T_i = |\mathcal{W}_i|$. Define
 297 $A_{ff}^{(i)}$ as A_{ff} restricted (in rows and columns) to the sparsity pattern \mathcal{W}_i , and $a_{fc}^{[i]}$ and $w^{[i]}$ as A_{fc} and
 298 W restricted to column i , respectively, with rows restricted to the sparsity pattern of \mathcal{W}_i . The standard
 299 ℓ AIR approach for finding each $w^{[i]}$ is then equivalent to solving: for each $i \in n_c$ solve

300 (3.1)
$$A_{ff}^{(i)} w^{[i]} = -a_{fc}^{[i]}.$$

301 If we consider solving (3.1) at each i , we can rewrite the procedure as the following global block diagonal
 302 system, where we assume n_c points on the coarse grid:

303 (3.2)
$$A_{ff}^{(*)} w^{[*]} := \begin{bmatrix} A_{ff}^{(0)} & & & \\ & A_{ff}^{(1)} & & \\ & & \ddots & \\ & & & A_{ff}^{(n_c)} \end{bmatrix} \begin{bmatrix} w^{[0]} \\ w^{[1]} \\ \vdots \\ w^{[n_c]} \end{bmatrix} = - \begin{bmatrix} a_{fc}^{[0]} \\ a_{fc}^{[1]} \\ \vdots \\ a_{fc}^{[n_c]} \end{bmatrix} = -a_{fc}^{[*]}.$$

304 The solution of system (3.2) gives us classic AIR interpolation. As a side note, let W be stored in a
 305 sparse matrix format, then the global vector of all the nonzeros of W , denoted $w^{[*]}$, corresponds to the
 306 data array for the sparse representation of W when stored in compressed column format.

307 **3.1. Proposed Method with Global Constraints.** Given the above formulation of ℓ AIR in
 308 (3.2), we define the procedure for incorporating a global mode interpolation constraint into the approach.
 309 To enforce the mode interpolation constraint (2.13), define the matrix Q , such that $Qw^{[*]}$ is equivalent
 310 to PB_c , i.e., the entries of B_c populate Q such that the constraint equation (2.13) is equivalent to saying

311 (3.3)
$$Qw^{[*]} = \begin{bmatrix} B^{[0]}|_F \\ B^{[1]}|_F \\ \vdots \\ B^{[k]}|_F \end{bmatrix} = B^{[*]}|_F,$$

312 where $B^{[i]}$ is the i th column of B , $B^{[*]}$ represents the columns of B stacked vertically, and $B^{[*]}|_F$
 313 represents columns of B stacked vertically, but restricted to the fine-grid points F . Equation (3.3) is
 314 also equivalent to the constraint that $WB_c = B|_F$.

315 Thus our constrained minimization problem is

316 (3.4a)
$$\min_{w^{[*]}} \|a_{fc}^{[*]} + A_{ff}^{(*)} w^{[*]}\|_2$$

317 (3.4b) subject to $Qw^{[*]} = B^{[*]}|_F$.

319 This is an equality constrained minimization problem, with various solution approaches [14].

320 **3.1.1. Direct Solution to Minimization Problem.** The minimization problem (3.4a)–(3.4b)
 321 can be solved directly via the following Karush–Kuhn–Tucker (KKT) system

322 (3.5)
$$\begin{bmatrix} (A_{ff}^{(*)})^T A_{ff}^{(*)} & Q^T \\ Q & \mathbf{0} \end{bmatrix} \begin{bmatrix} w^{[*]} \\ \lambda \end{bmatrix} = \begin{bmatrix} -(A_{ff}^{(*)})^T a_{fc}^{[*]} \\ B^{[*]}|_F \end{bmatrix}.$$

323 The (1,1) block of equation (3.5) uses the normal equations, as the minimization principle requires an
 324 SPD matrix and we do not assume that $A_{ff}^{(*)}$ is SPD.

325 System (3.5) could be solved exactly via a Schur complement approach. If this is done, letting
 326 $\bar{A}^{-1} = \left((A_{ff}^{(*)})^T A_{ff}^{(*)} \right)^{-1}$, the solution is

327 (3.6)
$$w^{[*]} = (I - \bar{A}^{-1} Q^T (Q \bar{A}^{-1} Q^T)^{-1} Q) \bar{A}^{-1} (A_{ff}^{(*)})^T a_{fc}^{[*]} + (\bar{A}^{-1} Q^T (Q \bar{A}^{-1} Q^T)^{-1} Q^T)^{-1} B^{[*]}|_F,$$

329 where Q is the rectangular constraint matrix from above. Upon inspection, computing (3.6) is an
 330 expensive endeavour, especially $(Q \bar{A}^{-1} Q^T)^{-1}$ and potentially, the transpose of $A_{ff}^{(*)}$. To avoid these
 331 costs, we consider an iterative approach related to energy-minimization AMG [22].

332 **3.1.2. Iterative Solution to Minimization problem.** A review of approaches for obtaining
 333 an inexpensive iterative solution to (3.5) is given in [14]. One option previously used for AMG (e.g.,
 334 for root-node) is projected Krylov methods. Here, an initial guess (tentative interpolation) $w^{[*],t}$ that
 335 satisfies the constraints is constructed, so that $Qw^{[*],t} = B^{[*]}|_F$. Then, a projected Krylov method using
 336 Q is applied to solve the interpolation equation (3.2). The inverse $(Q\bar{A}^{-1}Q^T)^{-1}$ is not required and the
 337 transpose is not needed, because we only compute the residual for the interpolation equation (3.2) when
 338 computing a descent direction for equation (3.4a). The previous works [22, 19] use such a projected CG
 339 and GMRES approach for the symmetric and nonsymmetric cases, respectively. However as noted in
 340 Section 2.3, the nonsymmetric GMRES approach will approximate P_{ideal} in the constraint space for the
 341 normal equations, which is not desirable.

342 Thus here, we consider a simpler and cheaper linear iteration for minimizing (3.4a) that approximates
 343 P_{ideal} for the original operator in the constraint space. We find that this approach yields effective
 344 restriction and interpolation operators.

345 An additional cost consideration is whether or not to precondition such an iterative solve. Since
 346 the matrix $A_{ff}^{(*)}$ is block diagonal, each block could be inverted (or approximately inverted). Thus, we
 347 consider the use of approximate inverse preconditioners of the following form:

$$348 \quad (3.7) \quad A_{ff}^{(*),-1} \approx \widehat{A_{ff}^{(*),-1}} = \begin{bmatrix} \widehat{A_{ff}^{(0),-1}} & & & \\ & \widehat{A_{ff}^{(1),-1}} & & \\ & & \ddots & \\ & & & \widehat{A_{ff}^{(n_c),-1}} \end{bmatrix},$$

349 where $\widehat{A_{ff}^{(i),-1}}$ represents an approximate inverse to that block. Importantly, this inverse is *local* and can
 350 be generated in a variety of ways, e.g., diagonal, GMRES, or ILU approximations to each individual
 351 block inverse. This is *in contrast* to the “classic” energy-minimization which uses a single global Krylov
 352 polynomial to simultaneously approximate all block inverses. It is our belief that the block inverse
 353 approach is more effective. In particular, a global Krylov polynomial effectively assumes that each
 354 block has the same minimizing polynomial, whereas in reality each block will likely have its own unique
 355 minimizing polynomial (distinct from other blocks). The local approach allows us to calculate more
 356 accurate local inverses faster through locally accurate approximations and polynomials, or to solve each
 357 local equation directly.

358 **3.1.3. Proposed Algorithm for Computing R and P .** We now present our simple iterative
 359 scheme for minimizing (3.4a)–(3.4b) in Algorithm 3.1. The approach is a projected one-step iteration,
 360 which iteratively finds AIR-like interpolation operators with constraints. For restriction, the simplest
 361 approach on paper applies Algorithm 3.1 to A^T . However if forming a transpose is computationally
 362 expensive, one can also reformulate Algorithm 3.1 relative to $RA = 0$, as in the original ℓ AIR method [20].
 363 Then, the algorithm will still extract small submatrices $A_{ff}^{(i)}$, but after the extraction these submatrices
 364 will be transposed.

365 As input, the algorithm takes the operator A and corresponding strength of connection matrix S .
 366 Unless noted otherwise, we use the classical strength measure [24]. The input sparsity degree pattern
 367 m determines how wide the sparsity pattern in P will be, with $m = 1$ corresponding to distance-one
 368 interpolation based on the sparsity pattern of S_{fc} . Most commonly, we will use $m = 2$, which expands
 369 the sparsity to consider degree-two connections, similarly to ℓ AIR and root-node. Next, the input
 370 “Coarsen type” considers whether a classical “FC” coarsening, e.g., Ruge-Stüben coarsening [24], or an
 371 aggregation-based coarsening is used.

372 The coarsen type controls the base sparsity pattern for P . If classical FC coarsening is used, then the
 373 base pattern T comes from the FC rows of the strength matrix, S_{fc} . If an aggregation-based coarsening
 374 is used, which is significantly more aggressive, then the “Aggregation Operator”² is used for T . This

² The “Aggregation Operator” is generated by the algorithm from [30]. First, an aggregation (disjoint splitting) is computed with a greedy graph algorithm that finds the next degree-of-freedom (root node) with all unmarked neighbors and places those degrees-of-freedom in an aggregate and then marks them. A clean-up phase takes all unmarked degrees-of-freedom and places them in an adjacent aggregate. The root node of each aggregate is treated as a C-point. This procedure produces a CF-splitting that is significantly more aggressive (fewer C-points) than is typical for classical AMG

375 base pattern T is then expanded based on the strength of connection matrix S via $m - 1$ multiplications
 376 in line 13. We note that basing the interpolation pattern on strong connections is the same strategy as
 377 used by ℓ AIR and root-node, and this approach allows us to generate nearly identical patterns.

378 The least squares solution for line 15 is computed using a psuedoinverse based on B_c restricted to
 379 the sparsity pattern of row i , $w^{\{i\},t}$. These pseudoinverses can be locally precomputed for efficiency and
 380 are typically small.

381 The projection operation in line 19 takes each new update $\bar{w}^{[*]}$ and projects it so that $Q\bar{w}^{[*]} = 0$.
 382 That is, this operation ensures that each update $\bar{w}^{[*]}$ does not disturb the mode interpolation relationship
 383 $Qw^{[*,t]} = B^{[*,t]}|_F$. The projection operation with Q can be implemented locally using the same strategy
 384 as for line 15 (see [22]).

Algorithm 3.1 C ℓ AIR Algorithm

1: **Input:** A : Matrix
 2: S : Strength matrix for interpolation
 3: B : User supplied mode constraint vector(s)
 4: m : Sparsity pattern degree
 5: FC or Agg: Coarsening type
 6: **Output:** P : Interpolation in the form of the weight block $w^{[*,t]}$
 7: **set** tentative prolongation $w^{[*,t]}$, corresponding to $[-A_{fc}, I]$
 8: **set** base sparsity pattern T based on coarsening type
 9: **if** Coarsen type is FC
 10: $T \leftarrow [S_{fc}, I]$
 11: **else if** Coarsen type is Agg
 12: $T \leftarrow$ Aggregation Operator
 13: **set** expanded sparsity pattern to match F-row structure of $S^{m-1}T$
 14: $\mathcal{W} \leftarrow$ sparsity_pattern $((S^{m-1}T)|_F)$
 15: **expand** $w^{[*,t]}$ to store (possibly zero) entries for every nonzero in \mathcal{W}
 16: **enforce** constraints on $w^{[*,t]}$ such that $Qw^{[*,t]} = B^{[*,t]}|_F$, by taking row i , $w^{\{i\},t}$, and computing
 $w^{\{i\},t} \leftarrow$ least squares solution to $w^{\{i\},t}B_c = B$
 17: **compute** exact or approximate block inverses for $\widehat{A_{ff}^{(*),-1}}$
 18: **for** $k = 1, 2, \dots$ **do**
 19: **compute residual update** to minimize equation (3.4a), using $\mathbf{0}$ initial guess for $\bar{w}^{[*]}$:

$$\bar{w}^{[*]} \leftarrow \widehat{A_{ff}^{(*),-1}} \left(\left(-a_{fc}^{[*]} - A_{ff}^{(*)} w^{[*,t]} \right) - A_{ff}^{(*)} \mathbf{0} \right)$$

20: **project update:** $w^{[*]} \leftarrow (I - Q^T (Q Q^T)^{-1} Q) \bar{w}^{[*]}$
 21: **update interp:** $w^{[*,t]} \leftarrow w^{[*,t]} + \bar{w}^{[*]}$
 22: **end for**
 23: **set** final interpolation weights: $w^{[*]} \leftarrow w^{[*,t]}$
 24: **Return** $w^{[*]}$

385 *Remark 3.1.* If the constraints are removed from Algorithm 3.1 and the exact inverse $A_{ff}^{(*),-1}$ is used,
 386 then ℓ AIR is recovered. That is, removing the constraint lines 15 and 19 and assuming $k = 1$ yields the
 387 final update in line 20 of

388 $w^{[*,t]} \leftarrow w^{[*,t]} + w^{[*,1]}$
 389 $\leftarrow w^{[*,t]} + A_{ff}^{(*),-1} \left(-a_{fc}^{[*]} - A_{ff}^{(*)} w^{[*,t]} \right)$
 390 $\leftarrow -A_{ff}^{(*),-1} a_{fc}^{[*]}$

or rAMG. The “Aggregation Operator” is then a binary matrix where column i corresponds to aggregate i (i.e., the i th C-point) and this column is nonzero only for the degrees-of-freedom in aggregate i . See also [19] which constructs initial sparsity patterns in this manner.

392 However, we always use the constraints in Algorithm 3.1, making $\mathcal{C}\ell\text{AIR}$ distinct from ℓAIR .

393 *Remark 3.2.* We will most often use the exact inverse $A_{ff}^{(*),-1}$ for $\widehat{A_{ff}^{(*),-1}}$ in line 16, similar to ℓAIR .
394 In this case, Algorithm 3.1 is run with $k = 1$, i.e., the output of the algorithm does not change for $k > 1$.

395 **3.1.4. Comparison to Root-node.** We now clearly distinguish the similarities and differences
396 between $\mathcal{C}\ell\text{AIR}$ and root-node. The $\mathcal{C}\ell\text{AIR}$ approach shares with root-node (i) the same mode and
397 sparsity constraints (2.13) and (2.11), (ii) the ability to iteratively find P , and (iii) approximates some
398 form of P_{ideal} .

399 Regarding differences, root-node uses a simple diagonal approximation to A_{ff}^{-1} , whereas $\mathcal{C}\ell\text{AIR}$ uses
400 a potentially much more powerful approximation $\widehat{A_{ff}^{(*),-1}}$, where each block is often inverted exactly³.
401 The proposed $\mathcal{C}\ell\text{AIR}$ method also uses a simple one-step iteration that is cheaper computationally
402 than root-node, with no required global storage of Krylov vectors or the additional computations and
403 communications required to maintain the (globally) orthogonal Krylov basis. Lastly, root-node has only
404 considered fast aggregation-based coarsening, whereas $\mathcal{C}\ell\text{AIR}$ will support and explore both fast and
405 slow coarsening, targeting diffusive and advective problems, respectively.

406 **4. Numerical Results.** We now present supporting numerical results for $\mathcal{C}\ell\text{AIR}$, comparing
407 against root-node and ℓAIR for a variety of classic model diffusion problems and for advection-diffusion
408 problems over a range of diffusion parameters. The proposed solver is shown to (i) achieve more de-
409 sirable operator complexities than ℓAIR , (ii) compare well against the root-node solver for symmetric
410 diffusion problems, where root-node is already known to perform well, and (iii) be more robust regarding
411 parameter tuning when compared to ℓAIR , e.g., for the advection-diffusion problems when going from
412 the purely advective to highly diffusive regimes.

413 Our basic test framework is as follows. The ℓAIR and root-node solvers use the library implemen-
414 tations in PyAMG [3] and $\mathcal{C}\ell\text{AIR}$ is also implemented in PyAMG⁴. We use V(1,1) cycles as a preconditioner
415 for CG and GMRES in the symmetric and nonsymmetric settings, respectively. The smoother choices
416 respect the reduction framework. For presmoothing, we use 1 iteration of CFF-weighted-Jacobi, i.e.,
417 one Jacobi sweep on the C-points, followed by two Jacobi sweeps on the F-points. The weight is equal
418 to $1/\rho(D^{-1}A)$. (Here, $\rho(\cdot)$ denotes the spectral radius, which is approximated numerically by 15 it-
419 erations of Arnoldi.) For postsmoothing, we use 1 iteration of FFC-weighted-Jacobi, which is defined
420 analogously to CFF. Such relaxation methods are chosen for simplicity, parallelism, and the preserva-
421 tion of a symmetric preconditioner when A is symmetric, so that CG can be used. The absolute halting
422 criteria is 10^{-9} for the smallest problem size, and is then scaled to simulate a discrete L2-norm⁵. We
423 report preconditioned Krylov iterations and work-per-digit of accuracy. One work unit is defined to be
424 the cost of a fine-grid matrix-vector product, and work-per-digit of accuracy estimates how many work
425 units are required to reduce the residual by one order of magnitude. Work measurements allow for easy
426 comparison across methods. To derive our work-per-digit measure, we first estimate the total cost of
427 doing one matrix-vector product at each level in the hierarchy, relative to one matrix-vector product on
428 the finest level. This yields the operator complexity measure

429 (4.1)
$$\text{OC} = \sum_k \text{nnz}(A_k)/\text{nnz}(A_0),$$

430 where A_k is the operator on level k in the multigrid hierarchy and $\text{nnz}(\cdot)$ stands for the number of
431 nonzero entries. To account for the cost of doing relaxation at each level, we multiply OC by 3.5 because
432 we estimate (roughly) the cost of CFF- and FFC-Jacobi to be slightly less than 4 matrix-vector products.
433 Thus work-per-digit of accuracy is estimated as

434 (4.2)
$$\text{wpd} = 3.5 \text{ OC} / \log_{10}(\gamma),$$

435 where the average residual convergence factor is $\gamma = (\|r\|_k/\|r_0\|)^{1/k}$, r_k is the final residual, and r_0 is
436 the initial residual.

³Note that $\mathcal{C}\ell\text{AIR}$ also supports using a diagonal inverse similar to root-node, where each block of $\widehat{A_{ff}^{(*),-1}}$ would be the local diagonal inverse. However, this approximation does not always lead to effective AMG hierarchies in our experiments, e.g., for the 3D Poisson problem. Developing more effective approximations is future research.

⁴The $\mathcal{C}\ell\text{AIR}$ implementation is in the `CF_rootnode` branch, commit `bf56195b55a27bd99625c385ee9ba1df8814f764`.

⁵In 2D, the tolerance is scaled by 2 each grid refinement, and in 3D, by $\sqrt{8}$.

437 **4.1. Diffusion Tests.** For the symmetric case, we consider a variety of classic diffusion tests.

438 **2D Poisson.** The PDE here is $-\mathbf{u}_{xx} - \mathbf{u}_{yy} = f$, with Dirichlet boundary conditions on the unit
439 box. The discretization is classic second-order 5-point finite differencing on a regular grid.

440 **3D Poisson.** The PDE here is $-\mathbf{u}_{xx} - \mathbf{u}_{yy} - \mathbf{u}_{zz} = f$, with Dirichlet boundary conditions on the
441 unit box. The discretization is classic second-order 7-point finite differencing on a regular grid.

442 **2D Grid-Aligned Anisotropic Diffusion.** The PDE here is

443 (4.3a) $-\nabla \cdot Q^T D Q \nabla u = f \quad \text{for } \Omega = [0, 1]^2,$

444 (4.3b) $u = 0 \quad \text{on } \partial\Omega,$

446 where Ω is the unit box domain and

447 (4.4)
$$Q = \begin{bmatrix} \cos(\varphi) & -\sin(\varphi) \\ \sin(\varphi) & \cos(\varphi) \end{bmatrix}, \quad D = \begin{bmatrix} 1 & 0 \\ 0 & \epsilon \end{bmatrix}$$

448 represent the rotation by angle φ and the strength of anisotropy ϵ . The discretization uses a regular grid
449 and bilinear (Q1) finite elements. For this problem $\varphi = 0$ and $\epsilon = 0.001$, representing strong grid-aligned
450 anisotropy in the x -direction.

451 **2D Rotated Anisotropic Diffusion.** Here the PDE and discretization are the same as for equa-
452 tions (4.3a)–(4.3b), but $\varphi = \pi/8$ and ϵ remains 0.001. This represents strong non-grid-aligned anisotropy
453 at the angle of $\pi/8$. As noted in [25, 15, 5], this is a difficult discretization and angle of anisotropy for
454 AMG.

455 **Box-in-Box Coefficient Jump.** The PDE here is

456 (4.5a) $-\nabla \cdot d(x, y) \nabla u = f \quad \text{for } \Omega,$

457 (4.5b) $u = 0 \quad \text{on } \partial\Omega,$

459 where $d(x, y)$ is the jumping coefficient. Here, $\Omega = [0, 1]^2$, $d(x, y) = 1$ if $(x, y) \notin [0.44, 0.52]^2$, and
460 $d(x, y) = 10^4$ if $(x, y) \in [0.44, 0.52]^2$. The grid is regular and the coefficient jumps are grid-aligned
461 on the finest level, but will not be grid-aligned at coarser levels due to the algebraic coarsening. The
462 discretization is classic second-order 5-point finite differencing from [1] for coefficient jump problems.

463 **Sawtooth Coefficient Jump.** Here, the PDE and discretization are the same as for equations
464 (4.5a)–(4.5b), but $\Omega = [0, 16]^2$, $d(x, y) = 1$ for points outside the shaded region of Figure 1, and
465 $d(x, y) = 10^4$ for points inside the shaded region [1].

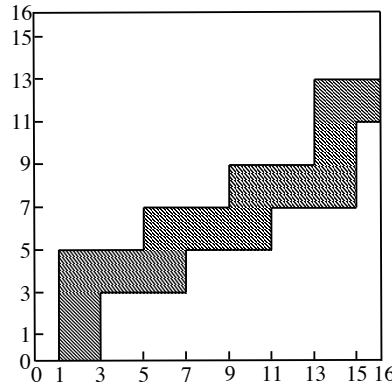


Fig. 1: Sawtooth coefficient jump domain, $d(x, y) = 10^4$ in shaded region and $d(x, y) = 1$ outside.

465

466 **Laplace Problem with Adaptive Mesh Refinement (AMR).** Here, we consider a finite ele-
467 ment discretization of the Laplace problem $-\Delta u = 1$ with homogeneous Dirichlet boundary conditions.
468 This problem is solved on a sequence of meshes in an \mathbb{H}^1 -conforming finite element space which are

469 locally refined in accordance with a simple Zienkiewicz-Zhu [33] error estimator. We save the stiffness
 470 matrix A throughout each iteration of the AMR loop and use this matrix to further illustrate differences
 471 in outcomes across various AMG solvers. This example is identical to PyMFEM library example 6
 472 [2, 23]. AMR stages for the star mesh file used in this problem are shown in Figure 2.

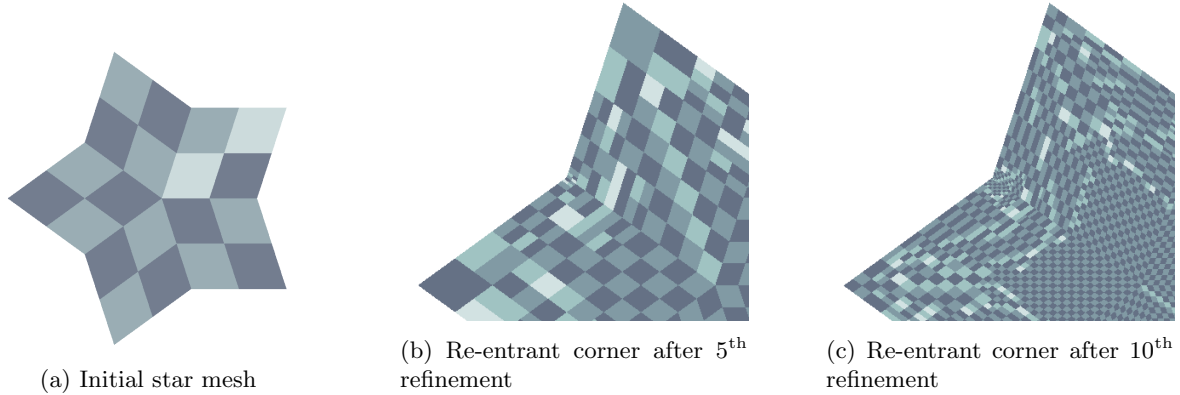


Fig. 2: AMR throughout different stages for the Laplace problem.

473 **Standard Solver Parameters.** We now list our standard solver parameters for all three methods,
 474 ℓ AIR, $C\ell$ AIR, and root-node. We will occasionally tune the parameters (e.g., strength) for ℓ AIR and
 475 root-node, in order to make the existing methods more competitive. The parameters for the proposed
 476 $C\ell$ AIR method will remain fixed for all symmetric test cases, except for the 2D Rotated Anisotropic
 477 Diffusion case, where we will follow the guidance of [25] and consider larger degree interpolation sparsity
 478 patterns. We use accelerated CG for $C\ell$ AIR and root-node and accelerated GMRES for ℓ AIR, as the
 479 typical approach for ℓ AIR is not symmetric (i.e., does not satisfy $R = P^T$, see below parameter choices).

480 *Parameters for ℓ AIR* (see [20] for more details on parameter definitions)

- 481 – Strength-of-connection tolerance for coarsening 0.25
- 482 – Degree 2 ℓ AIR restriction (sparsity pattern similar to $m = 2$ in Algorithm 3.1) with interpolation
 483 strength tolerance 0.05
- 484 – Ruge-Stüben coarsening first-pass only [24] (coarsen type FC in Algorithm 3.1, relatively slow
 485 coarsening often used by ℓ AIR)
- 486 – Coarse-grid matrices filtered with drop-tolerance of 10^{-4}
- 487 – Classical interpolation formula used for P [24], which is typical for ℓ AIR and diffusive problems

488 *Parameters for $C\ell$ AIR*

- 489 – Strength-of-connection tolerance for coarsening 0.5
- 490 – Degree 2 sparsity pattern for P ($m = 2$ in Algorithm 3.1) with interpolation strength tolerance 0.5
 491 used to generate S in Algorithm 3.1
- 492 – Mode constraint vector $B = \mathbf{1}$, presmoothed with 5 iterations of CFF-weighted-Jacobi at each level
- 493 – $R = P^T$ used (see discussion below)
- 494 – Aggregation based coarsening (coarsen type Agg in Algorithm 3.1)

495 *Parameters for root-node* (see [19] for more parameter details)

- 496 – Strength-of-connection tolerance for coarsening 0.25
- 497 – P smoothed with energy-minimizing projected CG and a degree 2 sparsity pattern (sparsity pattern
 498 similar to $m = 2$ in Algorithm 3.1)
- 499 – Mode constraint vector $B = \mathbf{1}$, presmoothed with 5 iterations of Jacobi at each level
- 500 – $R = P^T$ used (see discussion below)
- 501 – Aggregation based coarsening (standard coarsening for root-node)

502 We note that the interpolation strength-of-connection tolerance for $C\ell$ AIR is different than that

503 for ℓ AIR (0.5 versus 0.05). Both of these tolerance were tuned individually for each method. We also
 504 note that $\mathcal{C}\ell$ AIR and root-node both use $R = P^T$, while ℓ AIR uses classical interpolation. The use
 505 of classical interpolation (instead of R^T , the transpose of ℓ AIR restriction) with ℓ AIR is typical for
 506 diffusive problems, and additionally, the use of R^T as interpolation leads to undesirably large operator
 507 complexities.

508 **4.1.1. Poisson Results.** We next examine convergence results for the 2D and 3D Poisson problems
 509 in Figure 3. Here, we tune ℓ AIR to obtain a more challenging baseline solver and set the sparsity pattern
 510 in R to degree 1. For these simplest of problems, this choice reduces the operator complexity, while not
 511 affecting convergence. For our other test problems, such a parameter choice does not lead to the best
 512 performance. Operator complexities over all test problems, which are an advantage of $\mathcal{C}\ell$ AIR, are
 513 discussed later in Section 4.1.3.

514 Figures 3a and 3c depict results for the 2D and 3D Poisson problems, respectively. Overall, we
 515 see flat iteration counts for all methods, except a slight growth for ℓ AIR in the 2D Poisson case. The
 516 chief performance difference is that ℓ AIR has a significantly higher operator complexity than $\mathcal{C}\ell$ AIR and
 517 root-node, which will be discussed in Section 4.1.3

518 Figure 3b demonstrates that $\mathcal{C}\ell$ AIR can also be run similar to ℓ AIR with Ruge-Stüben coarsening
 519 with first-pass only and classical interpolation for P . In general, this setup does not lead to the most
 520 efficient solver for $\mathcal{C}\ell$ AIR, due to the high operator complexity ($OC \approx 3.3$).

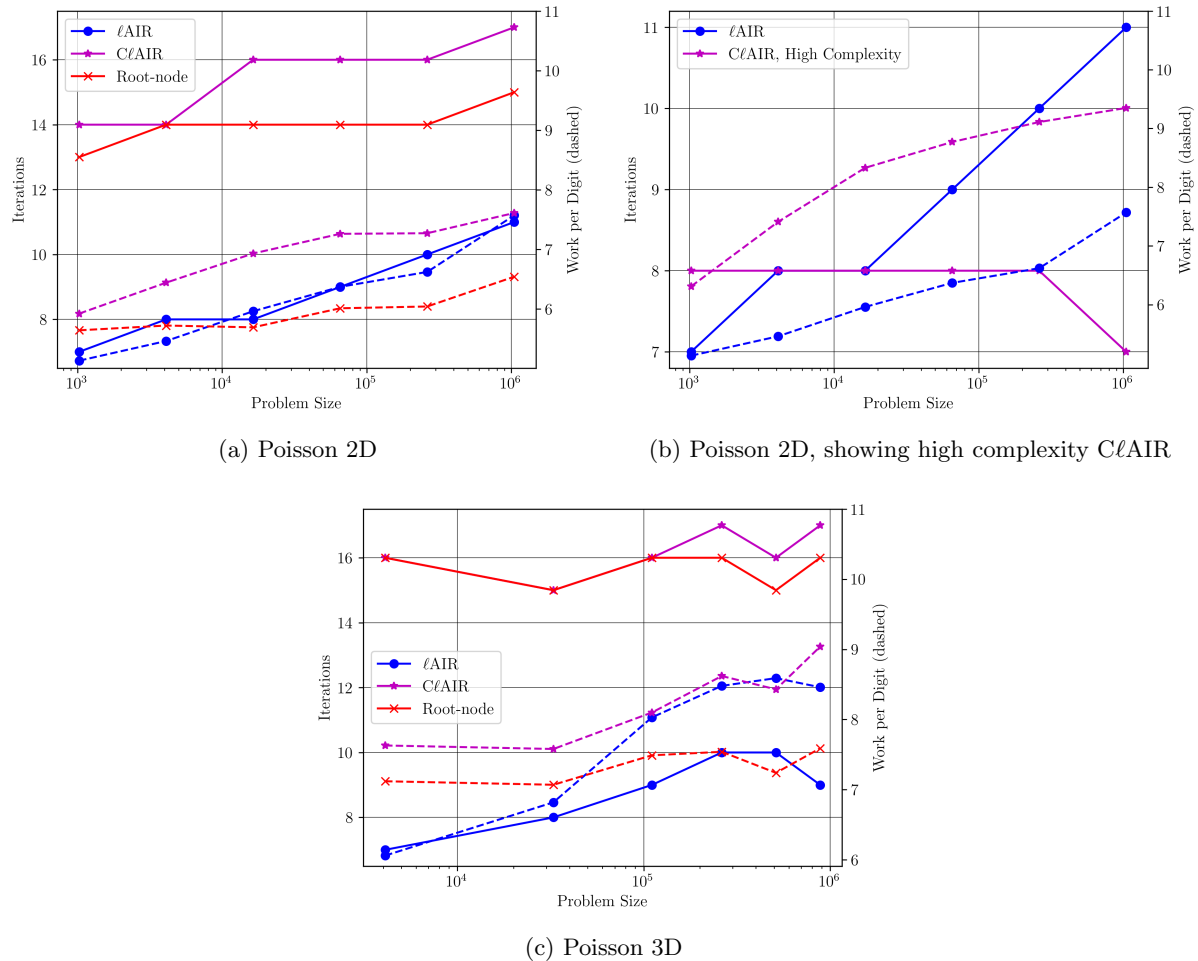


Fig. 3: 2D and 3D Poisson, comparison of iterations and work-per-digit of accuracy for ℓ AIR, $\mathcal{C}\ell$ AIR, and root-node.

521 **4.1.2. Other Diffusion Results.** We now consider our other diffusion test problems in Figure
 522 4, which again depicts iterations and work-per-digit of accuracy. For these tests, we tune root-node
 523 and ℓ AIR on the 2D Grid-Aligned Anisotropic Diffusion problem, in order to obtain more challenging
 524 baseline solvers. Here, we set the coarsening and interpolation strength-of-connection tolerances to 0.5
 525 and note that using such a high interpolation strength tolerance typically hurts ℓ AIR performance,
 526 with this case being the outlier. Thus, this is not a general parameter setting for ℓ AIR and is used to
 527 highlight the greater flexibility of the untuned $\mathcal{C}\ell$ AIR solver. Following the work [25], we also consider
 528 higher-degree interpolation for the 2D Rotated Anisotropic Diffusion case, for both root-node and $\mathcal{C}\ell$ AIR.
 529 Unfortunately, prohibitive increases in operator complexity for ℓ AIR do not allow for such an examination
 530 of higher-degree interpolation.

531 Figure 4a depicts results for the 2D Grid-Aligned Anisotropic Diffusion problem, where we see similar
 532 performance for $\mathcal{C}\ell$ AIR, root-node, and ℓ AIR. Figure 4b depicts results for the 2D Rotated Anisotropic
 533 Diffusion problem where all three solvers produce similar work-per-digit numbers, and the root-node
 534 and $\mathcal{C}\ell$ AIR solvers show flat, scalable iteration counts for the higher-degree interpolation option.

535 Figures 4c and 4d depict results for the Box-in-Box Coefficient Jump and Sawtooth Coefficient Jump
 536 problems. All three solvers again show similar work-per-digit numbers, with the main difference being
 537 in operator complexity, which we discuss in the next subsection.

538 Finally, results for the Laplace problem with AMR utilizing an unstructured star mesh are shown in
 539 Figure 4e. While $\mathcal{C}\ell$ AIR and root-node performance are comparable in this instance, ℓ AIR shows high
 540 preconditioned iterations and work-per-digit accuracy as problem size increases. ℓ AIR performance may
 541 be improved by raising the strength-of-connection tolerance from 0.25 to 0.5 and adding the second pass
 542 of Ruge-Stüben coarsening, resulting in a maximum of 25 preconditioned iterations. However, in doing
 543 so, the operator complexity becomes prohibitively high at around 3.88. Lastly, we note that the work
 544 per digit for $\mathcal{C}\ell$ AIR and root-node grows slowly for this problem as the mesh is adaptively refined, but
 545 we do not find this surprising given the re-entrant corners and adaptive refinement. We also observed a
 546 similar slow growth when using the benchmark classical Ruge-Stüben solver for this problem.

547 **4.1.3. Operator Complexity Comparison.** One key advantage for $\mathcal{C}\ell$ AIR when compared to
 548 other reduction-based approaches on diffusion problems is the ability to achieve moderate operator com-
 549 plexities with good convergence. To illustrate this, Table 1 depicts the operator complexity for all three
 550 solvers and the largest problem size for each of the diffusion test problems. Here, this advantage to $\mathcal{C}\ell$ AIR
 551 becomes obvious. The faster aggregation-based coarsening, which only root-node and $\mathcal{C}\ell$ AIR support,
 552 allows for dramatically lower operator complexities and the associated lower storage requirements.

553 Importantly, one could not simply introduce the aggregation-based coarsening into ℓ AIR and main-
 554 tain good convergence. The addition of the mode interpolation constraint vector B is needed for good
 555 convergence.

556 We note that the operator complexity of 1.98 for $\mathcal{C}\ell$ AIR and the 2D Rotated Anisotropic Diffusion
 557 case can easily be brought down to 1.78 without a meaningful effect on convergence by using 0.25 as the
 558 strength-of-connection tolerance, but we choose to maintain uniform parameters for $\mathcal{C}\ell$ AIR.

Test Problem	ℓ AIR OC	$\mathcal{C}\ell$ AIR OC	Root-node OC
2D Poisson	2.20	1.40	1.34
3D Poisson	2.87	1.71	1.57
2D Grid-aligned Anisotropic Diffusion	4.92	1.52	1.51
2D Rotated Anisotropic Diffusion	2.89	1.98	1.52
Box-in-Box Coefficient Jump	2.73	1.40	1.34
Sawtooth Coefficient Jump	2.71	1.42	1.35
Laplace Problem with AMR	2.03	1.32	1.17

Table 1: Operator complexities of ℓ AIR and $\mathcal{C}\ell$ AIR for different diffusion test problems.

559 **Remark 4.1.** In summary, we have shown that $\mathcal{C}\ell$ AIR performs similarly in terms of work-per-digit,
 560 operator complexity, and iterations on this suite of classic diffusion test problems when compared to
 561 root-node, an AMG method known to be efficient for such problems. Our goal is not to find a faster
 562 solver for the 5-point Poisson operator, which would be difficult and of questionable value, but instead to

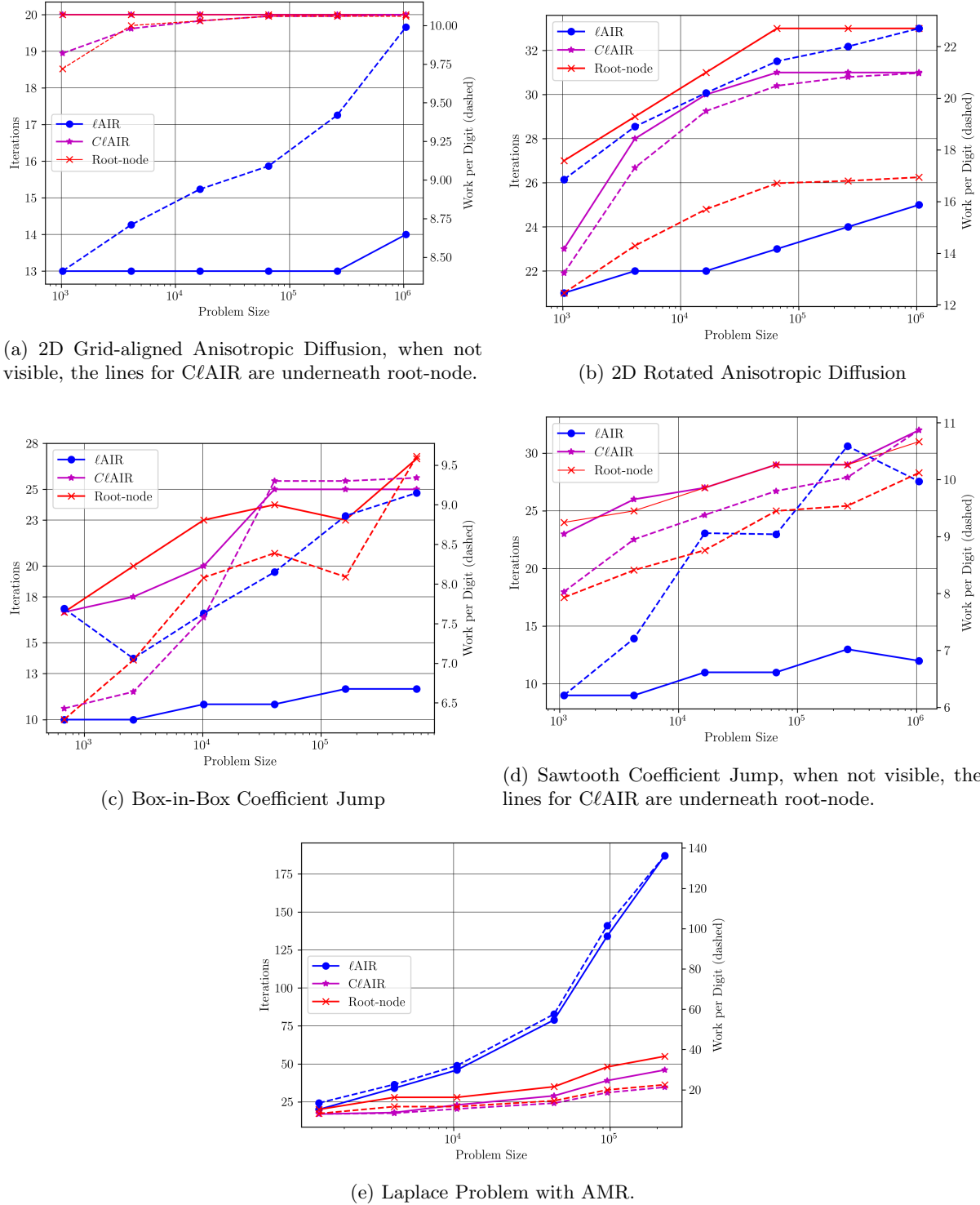


Fig. 4: Various diffusion test problems, comparison of iterations and work-per-digit of accuracy for ℓ AIR, $C\ell$ AIR, and root-node.

563 verify the proposed solver. We have furthermore shown greater parameter insensitivity and dramatically
 564 lower operator complexities when compared to ℓ AIR for these problems. Finally, it is important to
 565 highlight that $C\ell$ AIR retains good convergence and low operator complexity across a range of diffusion

566 problems, which has proven challenging for previous reduction-based approaches.

567 **4.2. Advection-Diffusion Tests.** We now turn our attention to nonsymmetric tests and consider
568 the following two advection-diffusion problems.

569 **2D Constant Direction Advection-Diffusion.** Here the PDE is

570 (4.6a)
$$-\alpha \nabla \cdot \nabla u + \mathbf{b}(x, y) \cdot \nabla u = f \quad \text{for } \Omega = [-1, 1]^2,$$

571 (4.6b)
$$u = 0 \quad \text{on } \partial\Omega,$$

573 where α is the diffusion constant and $\mathbf{b}(x, y)$ describes the advection. For this problem $\mathbf{b}(x, y) =$
574 $[\sqrt{2/3}, \sqrt{1/3}]$ representing constant non-grid-aligned advection. The discretization is first-order up-
575 winded discontinuous Galerkin (DG) for advection and the interior-penalty method for the DG dis-
576cretization of diffusion. The discretization was generating by utilizing examples 14 (diffusion) and 9
577 (advection) with PyMFEM [2, 23]. For the case where $\alpha = 0$, the boundary conditions are modified
578 slightly such that an outflow now occurs on the North and East walls ($u = 0$ is still prescribed on
579 the West and South walls). We use $u = 0$ for the inflow, so that we may test our solver with a zero
580 right-hand-side and random initial guess, as is commonly done to verify AMG solvers.

581 **2D Recirculating Advection-Diffusion.** Here the PDE and discretization is the same as for
582 equations (4.6a)–(4.6b), except $\mathbf{b}(x, y) = [x(1-x)(2y-1), -(2x-1)(1-y)y]$, representing divergence-
583 free recirculating advection about the origin. For $\alpha = 0$, this problem is ill-defined, thus we demonstrate
584 numerical results over a range of diffusion constants (α), starting from a smallest diffusion constant
585 $\alpha = 10^{-4}$ and going to $\alpha = 10.0$, so that we test the advective, mixed, and diffusive regimes.

586 **4.2.1. Advection-Diffusion Results.** Our goal here is to test the solver’s robustness from the
587 highly advective to highly diffusive regime and show improved performance and robustness relative to
588 the current state ℓ AIR. Similar to [20], we pre-scale the fine-grid matrices with the inverse of their
589 diagonal block (block-size equals the DG element size of 4). Our solver parameters will remain fixed
590 over these tests, and involve only minor changes to the symmetric parameters from Section 4.1. As
591 the matrices are nonsymmetric, GMRES is accelerated with V(1,1)-cycles. The relaxation weight for
592 postsmothing with FFC-Jacobi is removed, as we no longer need symmetry for our preconditioner and
593 this change slightly improves convergence for all methods.⁶ The parameters for ℓ AIR were changed
594 slightly to use the second pass of Ruge-Stüben coarsening. The parameters for $\mathcal{C}\ell$ AIR changed slightly
595 with the strength-of-connection parameters becoming the same as for ℓ AIR (0.25 for coarsening and 0.05
596 for interpolation). Additionally because of the nonsymmetry, P is generated separately from R using
597 A and A^T , respectively. We also again consider two variants of $\mathcal{C}\ell$ AIR, a high complexity version that
598 uses first pass only Ruge-Stüben coarsening, and lower complexity versions that uses aggregation-based
599 coarsening. The parameters for root-node changed similarly, where GMRES is now used for the energy-
600 minimization when computing P and P is generated separately from R using A and A^T , respectively.

601 Figure 5a depicts work-per-digit for the 2D Constant Direction Advection problem with no diffusion
602 ($\alpha = 0$). The purpose of this plot is to show that $\mathcal{C}\ell$ AIR enjoys similar convergence to ℓ AIR for this
603 test problem, where we know that ℓ AIR works well and is essentially the state-of-the-art [20].

604 Figures 5c and 5d depict for all three solvers (with two different variants of $\mathcal{C}\ell$ AIR) the work-per-
605 digit of accuracy over a range of diffusion (α) values for the constant direction and recirculating test
606 problems. The data points for root-node are omitted whenever the solver did not converge within 100
607 iterations (typically for small α values). We plainly see that $\mathcal{C}\ell$ AIR has the most consistent performance
608 in terms of work-per-digit accuracy across all regimes.

609 Table 2 highlights the operator complexity advantage of $\mathcal{C}\ell$ AIR over ℓ AIR for the constant advection
610 case (the recirculating free case is similar). For the more advective cases (smaller α), the high complexity
611 variant of $\mathcal{C}\ell$ AIR, using first-pass only Ruge-Stüben coarsening, obtains lower operator complexities of
612 roughly 15–30%, while for the more diffusive cases (larger α), the lower complexity variant of $\mathcal{C}\ell$ AIR,
613 using aggregation based coarsening, obtains operator complexities roughly 1.6x–2.5x smaller. In both
614 settings, significant storage savings are achieved.

615 *Remark 4.2.* For these plots, our goal is to highlight the robustness (lack of need for tuning) for
616 the $\mathcal{C}\ell$ AIR solver. Thus, we searched for good general parameters for each solver and held them fixed

⁶The removal of the weight also more closely follows the reduction point-of-view in that post-smoothing should primarily solve the F-equations, so the slight improvement of convergence is not surprising.

α	10.0	1.0	0.1	0.01	0.001	0.0001	0.0
ℓ AIR	3.19	3.19	3.20	3.19	3.70	3.19	4.28
$C\ell$ AIR, High Complexity	3.00	2.97	2.94	2.81	2.89	2.69	3.06
$C\ell$ AIR	1.28	1.29	1.29	1.96	DNC	DNC	DNC
Root-node	1.20	1.20	1.20	1.42	DNC	DNC	DNC

Table 2: Operator complexities of ℓ AIR and $C\ell$ AIR for different diffusion α values and the constant advection test problem. Entries “DNC” indicate the solver did not converge within 100 iterations.

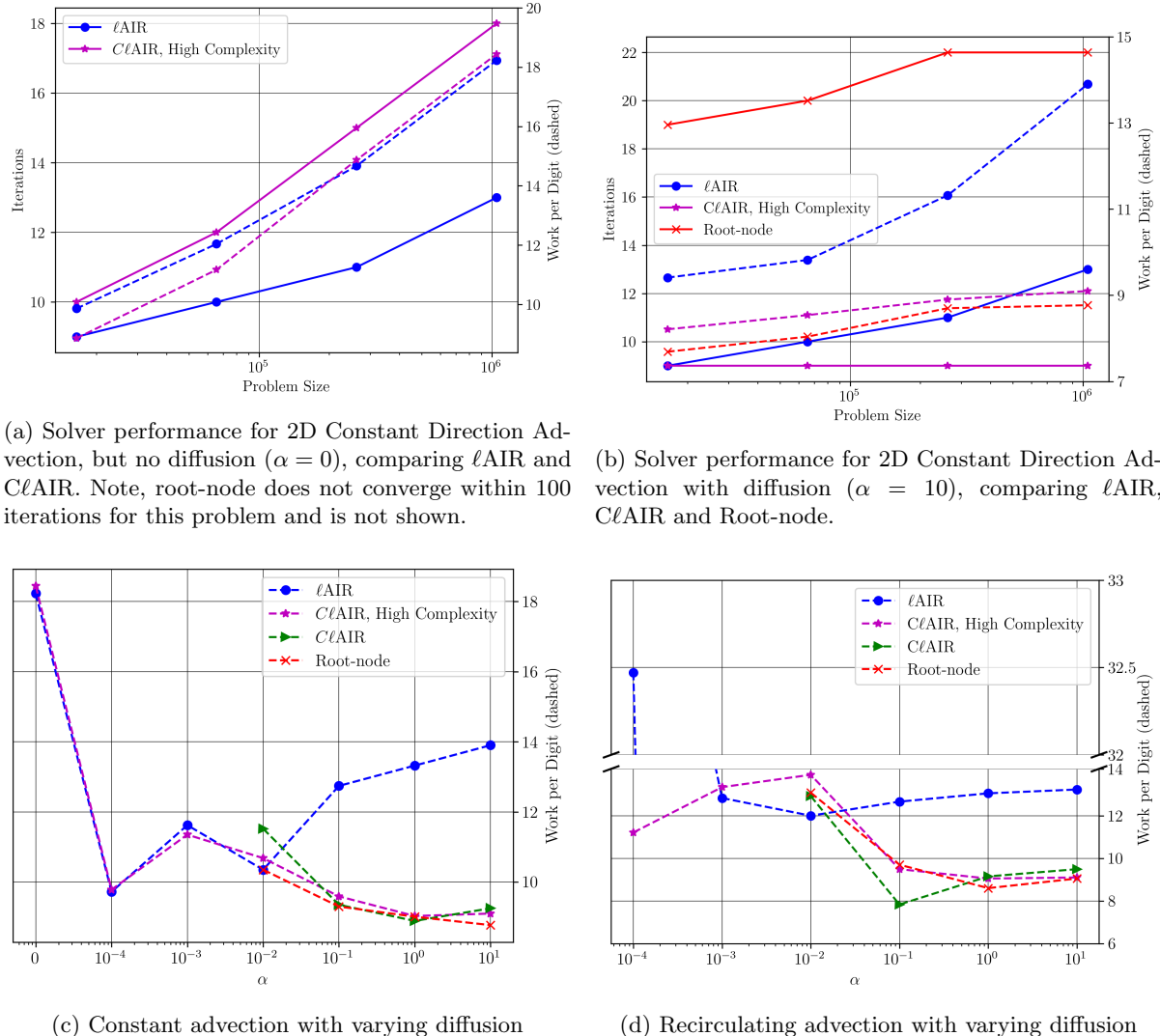


Fig. 5: Advection-diffusion problems, comparison of iterations, work-per-digit of accuracy and operator complexity for ℓ AIR, $C\ell$ AIR and Root-node.

617 over all tests. However, better parameters for individual problems and ℓ AIR do exist. For instance, if
 618 the matrix is *not* block diagonally pre-scaled, then the solver iterations and work for ℓ AIR in Figure
 619 Figure 5b ($\alpha = 10$ case) improve and become 7, 8, 8, 9 and 10.35, 10.43, 11.60, 11.81, respectively, but with
 620 a prohibitively large operator complexity of ~ 4.23 . However with no pre-scaling, the ℓ AIR then fails
 621 to converge within 100 iterations for the small α cases, e.g., Figure 5a. Another place where tuning is

622 beneficial for ℓ AIR is the smallest α value for the recirculating advection-diffusion problem ($\alpha = 10^{-4}$),
 623 where using first-pass only Ruge-Stüben coarsening lowers the iterations and work from 88 and 85.34 to
 624 21 and 15.86, respectively. However, the use of first-pass only Ruge-Stüben coarsening then substantially
 625 degrades iterations and work-per-digit results for ℓ AIR and other α values.

626 *Remark 4.3.* For a subset of the advection-diffusion problems considered in this section, Appendix
 627 A considers AMG approximation properties of $\mathcal{C}\ell$ AIR and ℓ AIR, with the results indicating that $\mathcal{C}\ell$ AIR
 628 either maintains or improves on the approximation properties of ℓ AIR.

629 In summary, the benefits of $\mathcal{C}\ell$ AIR are as follows. The ℓ AIR solver (i) requires more tuning for these
 630 problems than $\mathcal{C}\ell$ AIR, (ii) requires more work-per-digit than $\mathcal{C}\ell$ AIR for more diffusive problems (larger
 631 α values), and (iii) has significantly larger operator complexities.

632 **5. Conclusion.** In this paper, we developed a new type of reduction-based AMG that is suitable
 633 for solving nonsymmetric linear systems coming from the discretization of advection-diffusion PDEs. By
 634 combining techniques from ℓ AIR that have been effective for advective problems, with energy minimization
 635 and root node techniques that are well suited for diffusion problems, we have developed an efficient
 636 method for solving advection-diffusion problems in a general setting – the solver is insensitive to varying
 637 contribution of the diffusive part in the PDE. An important distinction between our proposed solver and
 638 existing reduction based methods is that we take a column-wise approach to computing an approximation
 639 to ideal restriction and interpolation, which more naturally allows us to incorporate energy minimization
 640 and mode constraint techniques into the process. Our future work focuses on deriving a two-grid
 641 convergence theory for the proposed approach applied to nonsymmetric systems and to incorporate the
 642 idea of compatible relaxation into the $\mathcal{C}\ell$ AIR coarsening process.

643 **Appendix A. Classical AMG Weak and Strong Approximation Properties.**

644 **A.1. Approximation Properties in the Nonsymmetric Setting.** We consider convergence
 645 of ℓ AIR and $\mathcal{C}\ell$ AIR based on classical multigrid weak and strong approximation properties. Targeting
 646 nonsymmetric problems, we consider the generalization of the A -norm as $\sqrt{A^*A}$ or $\sqrt{AA^*}$ [7, 21]. For
 647 a nonsingular matrix $A \in \mathbb{C}^{n \times n}$, consider the singular value decomposition (SVD) given by $A = U\Sigma V^*$
 648 where the singular values are $0 < \sigma_1 \leq \sigma_2 \leq \dots \leq \sigma_n$. Then $\sqrt{A^*A} = V\Sigma V^* = VU^*U\Sigma V^* = QA$ where
 649 $Q = VU^*$. In a similar manner, we can also obtain $\sqrt{AA^*} = U\Sigma U^* = AQ$. Since $\sqrt{A^*A}$ or $\sqrt{AA^*}$ are
 650 SPD matrices, therefore we can still consider classical AMG approximation properties with respect to
 651 the SPD matrices QA and AQ corresponding to the right and left singular vectors, respectively. Such
 652 approximation properties measure, in a sense, how effective the coarse spaces are at capturing the near
 653 nullspace of the operator.

654 For several test problems, we numerically evaluate approximation properties for ℓ AIR and $\mathcal{C}\ell$ AIR
 655 by making use of the generalized fractional approximation property (FAP) [21]. The FAP of a transfer
 656 operator $T \in \mathbb{R}^{n \times n_c}$ is with respect to the SPD matrix \mathcal{A} , with powers $\beta, \eta \geq 0$ and constant $K_{T,\beta,\eta}$.
 657 Specifically, T is said to have a FAP if for every fine grid vector, \mathbf{v} , there exists a coarse grid vector, \mathbf{v}_c ,
 658 such that

$$659 \quad (A.1) \quad \|\mathbf{v} - T\mathbf{v}_c\|_{\mathcal{A}^\eta}^2 \leq \frac{K_{T,\beta,\eta}}{\|\mathcal{A}\|^{2\beta-\eta}} \langle \mathcal{A}^{2\beta} \mathbf{v}, \mathbf{v} \rangle,$$

660 where $\mathcal{A} = QA$ ($T = P$) or $\mathcal{A} = AQ$ ($T = R^*$). The classical multigrid weak approximation property
 661 (WAP) is a FAP(1/2, 0), that is

$$662 \quad (A.2) \quad \|\mathbf{v} - T\mathbf{v}_c\|_2^2 \leq \frac{K_{T,1/2,0}}{\|\mathcal{A}\|} \langle \mathcal{A}\mathbf{v}, \mathbf{v} \rangle.$$

663 Further, the classical multigrid strong approximation property (SAP) is a FAP(1,1), that is

$$664 \quad (A.3) \quad \|\mathbf{v} - T\mathbf{v}_c\|_{\mathcal{A}}^2 \leq \frac{K_{T,1,1}}{\|\mathcal{A}\|} \langle \mathcal{A}^2 \mathbf{v}, \mathbf{v} \rangle.$$

665 For a given vector \mathbf{v} , we compute the approximation constant $K_{T,\beta,\eta}(\mathbf{v})$ with

$$666 \quad (A.4) \quad K_{T,\beta,\eta}(\mathbf{v}) = \frac{\|\mathcal{A}\|^{2\beta-\eta}}{\|\mathbf{v}\|_{\mathcal{A}^{2\beta}}^2} \min_{\mathbf{v}_c} \|\mathbf{v} - T\mathbf{v}_c\|_{\mathcal{A}^\eta}^2.$$

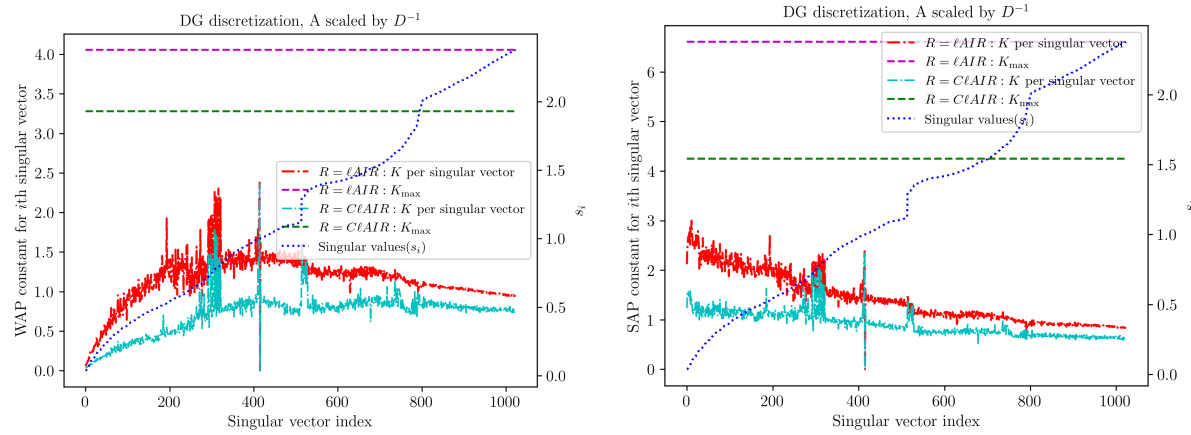
667 Let Π_η denote the \mathcal{A}^η -orthogonal projection onto the range of T , $\Pi_\eta = T(T^* \mathcal{A}^\eta T)^{-1} T^* \mathcal{A}^\eta$. Substituting
 668 into (A.4) we obtain,

669 (A.5)
$$K_{T,\beta,\eta}(\mathbf{v}) = \frac{\|\mathcal{A}\|^{2\beta-\eta}}{\|\mathbf{v}\|_{\mathcal{A}^{2\beta}}^2} \|(I - \Pi_\eta)\mathbf{v}\|_{\mathcal{A}^\eta}^2.$$

670 To compute the approximation constant K_{\max} that holds for all fine grid vectors \mathbf{v} , we take maximum
 671 of the above expression over all \mathbf{v} , which leads to

672 (A.6)
$$K_{\max} = \max_{\mathbf{v} \neq 0} K_{T,\beta,\eta}(\mathbf{v}) = \|\mathcal{A}\|^{2\beta-\eta} \|\mathcal{A}^{\eta/2}(I - \Pi_\eta)\mathcal{A}^{-\beta}\|_2^2.$$

673 **A.2. Numerical Tests.** To complement the numerical results in the main text, we now measure
 674 classical AMG approximation property constants for both ℓ AIR and $C\ell$ AIR from the purely advective to
 675 diffusion dominated case. Specifically, we consider the 2D constant direction advection problem (4.6a)–
 676 (4.6b) for various diffusion coefficients α . For numerical tests, a 32×32 size spatial domain is considered,
 677 resulting in 1024 total DOFs. In the following numerical tests, we consider the approximation properties
 678 of the restriction operators from both ℓ AIR and $C\ell$ AIR.



(a) WAP for Constant Advection with zero diffusion ($\alpha = 0$) where constraint vector $B = \mathbf{1}$ is presmoothed with 5 iterations of CFF-weighted-Jacobi.

(b) SAP for Constant Advection with zero diffusion ($\alpha = 0$) where constraint vector $B = \mathbf{1}$ is presmoothed with 5 iterations of CFF-weighted-Jacobi.

Fig. 6: WAP and SAP constants for the restriction operators of ℓ AIR and $C\ell$ AIR for the constant advection with zero diffusion ($\alpha = 0$) problem. Five (5) iterations of CFF-weighted-Jacobi relaxation has been used to improve the mode constraint vector $B = \mathbf{1}$ in $C\ell$ AIR. Singular values are shown in the dotted blue line and are associated with the right vertical axis, and the dot-dashed lines show the approximation constant for each of the left singular vectors of A . Horizontal dashed lines show the approximation constant for ℓ AIR and $C\ell$ AIR that holds for all vectors.

679 Figure 6 shows the WAP (FAP(1/2, 0)) and SAP (FAP(1, 1)) approximation constants for the left
 680 singular vectors of A . Here, 5 iterations of CFF-weighted-Jacobi relaxation has been used to improve
 681 the mode constraint vector $B = \mathbf{1}$. From Figure 6a and 6b, we see that $C\ell$ AIR demonstrates moderately
 682 smaller (i.e., better) WAP and SAP constants than ℓ AIR. Since ℓ AIR is primarily designed for such
 683 purely advective problems these results indicate that $C\ell$ AIR is also effective for advection problems,
 684 with similar convergence properties. This is indeed what we see in Figures 5a and 5c. This motivates
 685 us to further study approximation properties of $C\ell$ AIR for diffusion dominated problems.

686 Next, we consider a diffusion dominated case by setting the diffusion coefficient to be $\alpha = 10$. First,
 687 as previously, we use 5 iterations of a CFF-weighted-Jacobi smoother to improve the mode constraint
 688 vector $B = \mathbf{1}$. Carefully investigating the results in Figure 7a, we observe that WAP constant for the
 689 new method $C\ell$ AIR is almost a factor of two smaller than that for ℓ AIR. Now if we compare the SAP

constants in Figure 7b, K_{\max} is smaller for $\mathcal{C}\ell\text{AIR}$ than for ℓAIR , although the constants are very large for both solvers (184 for $\mathcal{C}\ell\text{AIR}$ and 2246 for ℓAIR). Somewhat surprisingly, while the SAP constant for $\mathcal{C}\ell\text{AIR}$ in Figure 7b is quite large, we find that the iteration counts of the solver are mesh independent (as we have seen in Figure 5b for the $\alpha = 10$ case). In this case, we suspect that the Krylov method is able to account for what the solver is lacking. We note that the significantly larger SAP constants for ℓAIR are consistent with the poorer scalability of ℓAIR seen in Figure 5b for the $\alpha = 10$ case. A key advantage of $\mathcal{C}\ell\text{AIR}$ is that it allows the flexibility to improve the approximation properties of the restriction operator by employing a suitable relaxation scheme for smoothing the mode constraint vector (such as weighted CFF-Jacobi). This type of flexibility is not available in ℓAIR . Therefore, further improvement of $\mathcal{C}\ell\text{AIR}$'s SAP constant can be obtained by increasing the number of iterations applied to B . In our experiments, we find that if the mode constraint vector $B = \mathbf{1}$ is presmoothed with 25 iterations of CFF-weighted-Jacobi (instead of 5 iterations), the SAP approximation constant for $\mathcal{C}\ell\text{AIR}$ decreases further to $K_{\max} = 77$ (Figure 7d). However, we do not find that these extra iterations lead to a meaningful improvement in practice for $\mathcal{C}\ell\text{AIR}$ convergence on the tested problems.

704 **Acknowledgments.** Los Alamos National Laboratory Report LA-UR-23-27101.

705

REFERENCES

- 706 [1] Raymond E Alcouffe, Achi Brandt, Joel E Dendy, Jr, and James W Painter. The multi-grid method for the diffusion equation with strongly discontinuous coefficients. *SIAM Journal on Scientific and Statistical Computing*, 2(4):430–454, 1981.
- 707 [2] Robert Anderson, Julian Andrej, Andrew Barker, Jamie Bramwell, Jean-Sylvain Camier, Jakub Cerveny, Veselin Dobrev, Yohann Dudouit, Aaron Fisher, Tzanio Kolev, Will Pazner, Mark Stowell, Vladimir Tomov, Ido Akkerman, Johann Dahm, David Medina, and Stefano Zampini. MFEM: A modular finite element methods library. *Computers & Mathematics with Applications*, 81:42–74, 2021.
- 708 [3] Nathan Bell, Luke N. Olson, Jacob Schroder, and Ben S. Southworth. PyAMG: Algebraic Multigrid Solvers in Python. *Journal of Open Source Software*, 2022. submitted.
- 709 [4] A. Brandt, S. McCormick, and J. Ruge. Algebraic multigrid (AMG) for automatic multigrid solution with application to geodetic computations. Technical report, Colorado State University, Fort Collins, Colorado, 1983.
- 710 [5] Achi Brandt, James Brannick, Karsten Kahl, and Ira Livshits. Algebraic distance for anisotropic diffusion problems: Multilevel results. *Electronic Transactions on Numerical Analysis*, 44:472–496, 2015.
- 711 [6] J. Brannick and L. Zikatanov. Algebraic multigrid methods based on compatible relaxation and energy minimization. In *Proceedings of the 16th International Conference on Domain Decomposition Methods*, volume 55 of *Lecture Notes in Computational Science and Engineering*, pages 15–26. Springer, 2007.
- 712 [7] Marian Brezina, T Manteuffel, S McCormick, J Ruge, and Geoffrey Sanders. Towards adaptive smoothed aggregation (α SA) for nonsymmetric problems. *SIAM Journal on Scientific Computing*, 32(1):14–39, 2010.
- 713 [8] S Dargaville, RP Smedley-Stevenson, PN Smith, and CC Pain. AIR multigrid with GMRES polynomials (AIRG) and additive preconditioners for Boltzmann transport. *arXiv preprint arXiv:2301.05521*, 2023.
- 714 [9] Hans De Sterck, Robert D Falgout, Stephanie Friedhoff, Oliver A Krzysik, and Scott P MacLachlan. Optimizing multigrid reduction-in-time and parareal coarse-grid operators for linear advection. *Numerical Linear Algebra with Applications*, 28(4):e2367, 2021.
- 715 [10] VA Dobrev, Tz Kolev, N Anders Petersson, and Jacob B Schroder. Two-level convergence theory for multigrid reduction in time (MGRIT). *SIAM Journal on Scientific Computing*, 39(5):S501–S527, 2017.
- 716 [11] Robert D Falgout, Stephanie Friedhoff, Tz V Kolev, Scott P MacLachlan, and Jacob B Schroder. Parallel time integration with multigrid. *SIAM Journal on Scientific Computing*, 36(6):C635–C661, 2014.
- 717 [12] Robert D Falgout and Panayot S Vassilevski. On generalizing the algebraic multigrid framework. *SIAM Journal on Numerical Analysis*, 42(4):1669–1693, 2004.
- 718 [13] Andreas Frommer, Karsten Kahl, Scott P. MacLachlan, Ludmil T. Zikatanov, and James Brannick. Adaptive reduction-based multigrid for nearly singular and highly disordered physical systems. *Electronic Transactions on Numerical Analysis*, 37:276–295, 2010.
- 719 [14] Nicholas IM Gould, Mary E Hribar, and Jorge Nocedal. On the solution of equality constrained quadratic programming problems arising in optimization. *SIAM Journal on Scientific Computing*, 23(4):1376–1395, 2001.
- 720 [15] Karsten Kahl and Matthias Rottmann. Least angle regression coarsening in bootstrap algebraic multigrid. *SIAM Journal on Scientific Computing*, 40(6):A3928–A3954, 2018.
- 721 [16] Scott MacLachlan, Tom Manteuffel, and Steve McCormick. Adaptive reduction-based AMG. *Numerical Linear Algebra with Applications*, 13(8):599–620, 2006.
- 722 [17] Jan Mandel, Marian Brezina, and Petr Vanek. Energy optimization of algebraic multigrid bases. 1998. CU Denver Technical Report.
- 723 [18] Thomas A Manteuffel, Steffen Münzenmaier, John Ruge, and Ben Southworth. Nonsymmetric reduction-based algebraic multigrid. *SIAM Journal on Scientific Computing*, 41(5):S242–S268, 2019.
- 724 [19] Thomas A Manteuffel, Luke N Olson, Jacob B Schroder, and Ben S Southworth. A root-node-based algebraic multigrid method. *SIAM Journal on Scientific Computing*, 39(5):S723–S756, 2017.
- 725 [20] Thomas A Manteuffel, John Ruge, and Ben S Southworth. Nonsymmetric algebraic multigrid based on local approximate ideal restriction. *SIAM Journal on Scientific Computing*, 40(6):A4105–A4130, 2018.
- 726 [21] Tom Manteuffel and Ben S Southworth. Convergence in norm of nonsymmetric algebraic multigrid. *SIAM Journal*

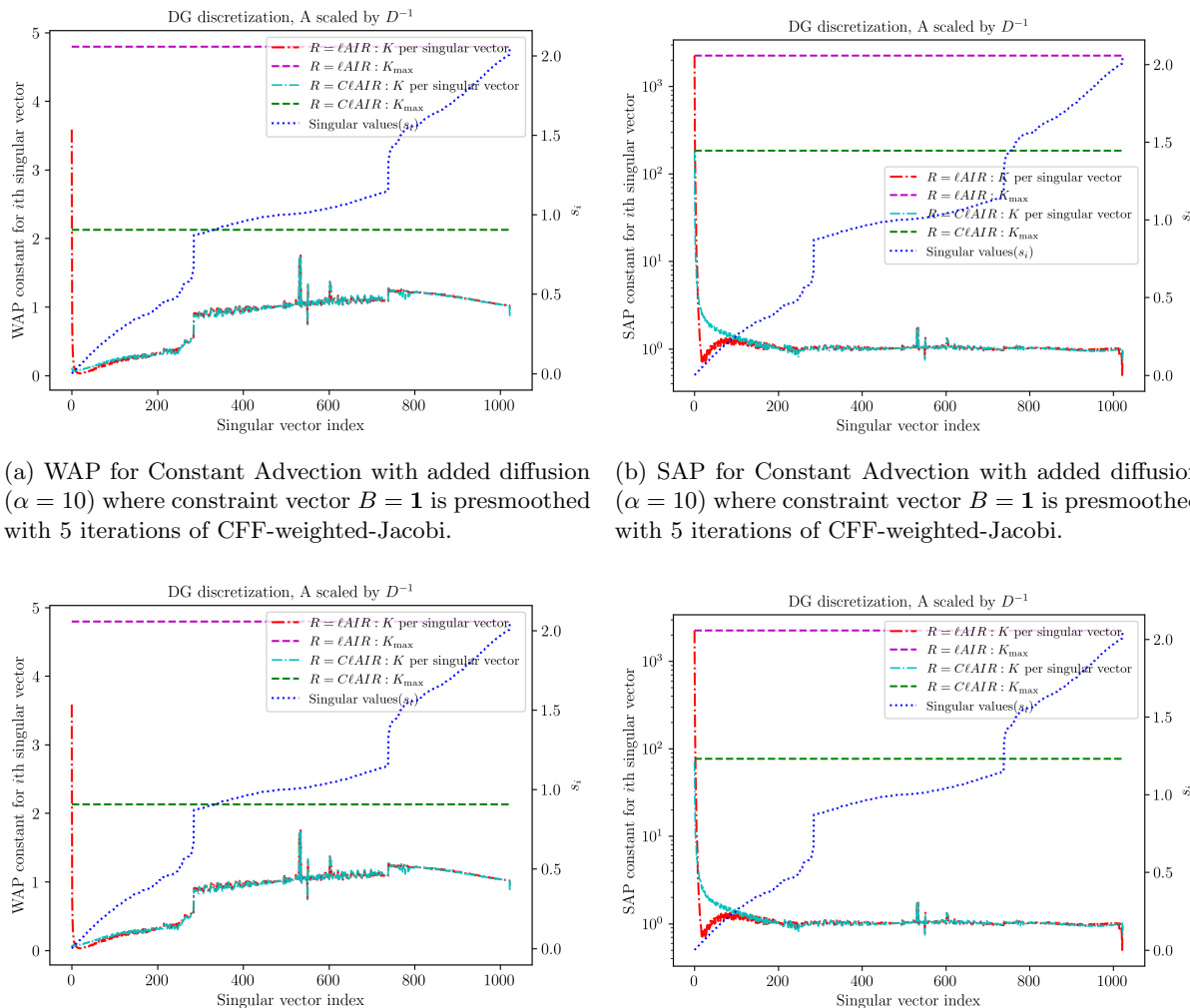


Fig. 7: WAP and SAP constants for the restriction operators of ℓ AIR and $\mathcal{C}\ell$ AIR for the constant advection with added diffusion ($\alpha = 10$) problem. Different number of iterations (5 and then 25) of CFF-weighted-Jacobi relaxation has been used to improve the mode constraint vector $B = \mathbf{1}$ in $\mathcal{C}\ell$ AIR. Singular values are shown in the dotted blue line and are associated with the right vertical axis, and the dot-dashed lines show the approximation constant for each of the left singular vectors of A . Horizontal dashed lines show the approximation constant for ℓ AIR and $\mathcal{C}\ell$ AIR that holds for all vectors.

on Scientific Computing, 41(5):S269–S296, 2019.

- [22] Luke N. Olson, Jacob B. Schroder, and Raymond S. Tuminaro. A general interpolation strategy for algebraic multigrid using energy minimization. *SIAM Journal on Scientific Computing*, 33(2):966–991, 2011.
- [23] PyMFEM. <https://github.com/mfem/PyMFEM/>.
- [24] J. W. Ruge and K. Stüben. Algebraic multigrid (AMG). In S. F. McCormick, editor, *Multigrid Methods*, volume 3 of *Frontiers in Applied Mathematics*, pages 73–130. SIAM, Philadelphia, PA, 1987.
- [25] J. B. Schroder. Smoothed aggregation solvers for anisotropic diffusion. *Numer. Linear Algebra Appl.*, 19:296–312, 2012.
- [26] Abdullah Ali Sivas, Ben S Southworth, and Sander Rhebergen. AIR algebraic multigrid for a space-time hybridizable discontinuous galerkin discretization of advection (-diffusion). *SIAM Journal on Scientific Computing*, 43(5):A3393–A3416, 2021.
- [27] Ben S Southworth. Necessary conditions and tight two-level convergence bounds for parareal and multigrid reduction in time. *SIAM Journal on Matrix Analysis and Applications*, 40(2):564–608, 2019.

766 [28] Ben S Southworth, Oliver Krzysik, and Will Pazner. Fast Solution of Fully Implicit Runge–Kutta and Discontinuous
767 Galerkin in Time for Numerical PDEs, part II: Nonlinearities and DAEs. *SIAM Journal on Scientific Computing*,
768 44(2):A636–A663, 2022.

769 [29] Ben S Southworth, Wayne Mitchell, Andreas Hessenthaler, and Federico Danieli. Tight two-level convergence of
770 linear parareal and MGRIT: Extensions and implications in practice. In *Parallel-in-Time Integration Methods: 9th Parallel-in-Time Workshop, June 8–12, 2020*, pages 1–31. Springer, 2021.

772 [30] P. Vaněk, J. Mandel, and M. Brezina. Algebraic multigrid based on smoothed aggregation for second and fourth
773 order problems. *Computing*, 56:179–196, 1996.

774 [31] W. L. Wan, Tony F. Chan, and Barry Smith. An energy-minimizing interpolation for robust multigrid methods.
775 *SIAM J. Sci. Comp.*, 21(4):1632–1649, 2000.

776 [32] Tareq Zaman, Nicolas Nytko, Ali Taghibakhshi, Scott MacLachlan, Luke Olson, and Matthew West. Generalizing
777 reduction-based algebraic multigrid. *arXiv preprint arXiv:2212.08371*, 2022.

778 [33] Olgierd Cecil Zienkiewicz and Jian Zhong Zhu. The superconvergent patch recovery and a posteriori error estimates.
779 part 2: Error estimates and adaptivity. *International Journal for Numerical Methods in Engineering*, 33(7):1365–
780 1382, 1992.